# Distributed representations of innate behaviors in the hypothalamus do not predict specialized functional centers

Stefanos Stagkourakis[1, *], Giada Spigolon[2], Markus Marks[3], Michael Feyder[4], Joseph Kim[1], Pietro Perona[3], Marius Pachitariu[5, #], David J. Anderson[1, 6, #, *]

[1] Division of Biology and Biological Engineering 156-29, Tianqiao and Chrissy Chen Institute for Neuroscience, California Institute of Technology, Pasadena, California 91125, USA

[2] Biological Imaging Facility, California Institute of Technology, Pasadena, California 91125, USA

[3] Division of Engineering and Applied Science, California Institute of Technology, Pasadena, California 91125, USA

[4] Division of Psychiatry and Behavioral Sciences, Stanford University, Palo Alto, California 94305, USA

[5] Howard Hughes Medical Institute, Janelia Research Campus, Ashburn, VA, USA

[6] Howard Hughes Medical Institute, California Institute of Technology, 1200 East California Blvd, Pasadena, California 91125, USA

[#] Joint supervision

* Corresponding authors: Stefanos Stagkourakis, David J. Anderson

E-mail: stefanos.stagkourakis@gmail.com, wuwei@caltech.edu

## Summary

Survival behaviors are orchestrated by hardwired circuits located in deep subcortical brain regions, most prominently the hypothalamus. Artificial activation of spatially localized, genetically defined hypothalamic cell populations is known to trigger distinct behaviors, suggesting a nucleus-centered organization of behavioral control. However, no study has investigated the hypothalamic representation of innate behaviors using unbiased, large-scale single neuron recordings. Here, using custom silicon probes, we performed recordings across the rostro-caudal extent of the medial hypothalamus in freely moving animals engaged in a diverse array of social and predator defense ("fear") behaviors. Nucleus-averaged activity revealed spatially distributed generic "ignition signals" that occurred at the onset of each behavior, and did not identify sparse, nucleus-specific behavioral representations. Single-unit analysis revealed that social and fear behavior classes are encoded by activity in distinct sets of spatially distributed neuronal ensembles spanning the entire hypothalamic rostro-caudal axis. Individual ensemble membership, however, was drawn from neurons in 3-4 adjacent nuclei. Mixed selectivity was identified as the most prevalent mode of behavior representation by individual hypothalamic neurons. Encoding models indicated that a significant fraction of the variance in single neuron activity is explained by behavior. This work reveals that innate behaviors are encoded in the hypothalamus by activity in spatially distributed neural ensembles that each span multiple neighboring nuclei, complementing the prevailing view of hypothalamic behavioral control by single nucleus-restricted cell types derived from perturbational studies.

## Introduction

Brains evolved to create a series of abstractions that represent objects or other sensory cues in an organism's environment, assess their value, predict impending changes in their features, and transform those signals into adaptive behavioral responses. To deconstruct this complex process, two main experimental strategies have been taken to either: 1) record neural activity during behavior, or 2) manipulate neural activity and observe changes in behavior. The first strategy starts with measurements of neuronal activity and correlates those data with manipulations and measurements of sensory features or task variables (*1-5*). The behavioral readouts typically involve artificial tasks that require intensive training and are highly reproducible across trials. In mammals, this strategy has been employed to study the cortex, hippocampus, or other evolutionarily recent areas (*6-10*), and their influence on cognitive functions.

The second strategy starts with surgical, electrical, neurochemical, or genetically-based perturbation experiments to identify brain regions and cell types whose activation, inhibition, or destruction can promote or suppress particular behaviors. These manipulations are targeted to pre-selected areas based on hypotheses, assumptions, or prior knowledge. This strategy has dominated the study of internal states, motivation, reward, and emotion (*11-15*). The behavioral readouts typically comprise innate behaviors or simple forms of conditioning based on such instincts. The study of such functions has typically focused on the so-called "limbic system," including evolutionarily ancient regions such as the extended amygdala (*16, 17*), hypothalamus (*18, 19*), and midbrain (*20, 21*).

The two above-mentioned strategies can yield fundamentally different views of the mechanisms underlying brain functions of interest. Although many studies in practice employ both strategies sequentially, prevailing views in a field are often strongly shaped by the approach that was initially undertaken (*22-24*). The "recording first" strategy has led to an emphasis on high-dimensional population codes, neural dynamics, and manifolds in cortico-hippocampal state-space. Nevertheless, the field is increasingly employing perturbation experiments to test hypotheses based on observational studies. In

contrast, the “perturbation first” strategy has led to an emphasis in the hypothalamus field on hard-wired neural circuits that causally control specific innate behaviors in a manner that is highly deterministic and low-dimensional (*25-27*). However, large-scale recording experiments in this field have been relatively rare.

It remains unclear, therefore, whether these different views of how cortical and limbic systems control behavior reflect true biological differences, or rather differences in the evolution of these fields according to the initial experimental strategies used at their inception. To help resolve this discrepancy, here we have performed large-scale recordings from neural populations located along the rostro-caudal axis of the medial hypothalamus, using custom-designed silicon probes in freely moving mice engaged in solitary, social, or predator-defense behaviors. Our results reveal that the neural coding of such instinctive behaviors is, surprisingly, more distributed, dynamic, and high-dimensional than would have been expected from perturbation experiments. These results invite a re-evaluation of views of neural coding principles in cortical vs. limbic areas and highlight the importance of integrating results from observational and perturbational studies to arrive at a comprehensive understanding of brain function.

# Results

## Recording single neurons across multiple sites of the hypothalamus during behavior

We sought to acquire synchronized large-scale electrophysiological and video recording data from freely moving mice engaging in diverse innate behaviors. To record the activity of hundreds of neurons simultaneously throughout the medial hypothalamus, we used a custom-fabricated silicon probe (NeuroNexus, Inc.) that allows chronic extracellular electrophysiological recordings (with single-unit resolution) from multiple nuclei (Fig. 1A). The eight-shank 256-channel silicon probe (Fig. 1B) was designed to provide simultaneous access to twenty hypothalamic subregions (nuclei or subnuclei), which are spatially distributed across the rostro-caudal extent of the hypothalamus (Fig. 1E). The probe covers ~2.3mm of brain tissue (Fig. 1A, lower), and we recorded ~400 units per animal (n=6 animals) for a total of 2,347 units.

To map shank trajectories, the back side of the probe shanks was coated with a red lipophilic dye that could be traced post-hoc. Intact iDISCO-cleared mouse brains were volumetrically imaged using light-sheet microscopy (*28*), and probe coordinates were mapped to the Allen Common Coordinate Framework (*29*) (Fig. 1, C and D). A unique electrode map was generated for each mouse by manually mapping electrodes to computationally sectioned sagittal sections of each mouse brain (Fig. S1 and S2). A schematic map of the areas recorded in each mouse is shown in Fig. 1E. Based on the electrode maps, neurons were allocated to specific hypothalamic brain areas (Fig. 1F, single-neuron activity colored according to the location of each neuron). Spike-sorting was performed using Kilosort (*30*), and basic analysis of neuron waveforms (Fig. 1G), and quality control of recordings was performed using pre-existing pipelines (see also Materials and Methods, section: *in vivo* electrophysiology). Neural data were analyzed in relation to behavior either a) with single neuron resolution (Fig. 1H – upper part), or b) by averaging the activity of cells per nucleus (Fig. 1H – lower part). This experimental design enabled us to test whether the encoding of behavior in the hypothalamus conforms to anatomical nuclear boundaries

and examine the extent to which neurons from the same nucleus are highly correlated or have distinct activity patterns across diverse behaviors. (Fig. 1I).

To investigate the representation of behavior in the hypothalamus, we grouped behaviors into three hierarchical levels (Fig 1I, right). At the highest level, we defined three broad behavioral categories which we refer to as “classes”: the solitary class includes actions such as self-grooming, and rearing. The social class includes behaviors such as sniffing a male or female conspecific, or attacking a male conspecific. The fear class includes behaviors such as sniffing a predator or exhibiting an escape response. At the second level, we distinguished two “domains” within the “social” class: intermale and male-female social behaviors (Fig. 1I, right; green and violet, respectively). Finally, at the third and lowest level, we annotated 43 distinct actions among the different classes and domains (Fig. 3B).

To ensure that the behaviors of interest would be expressed during the neural data recording sessions, animals (male Swiss-Webster mice) were pre-screened for robust performance in the relevant behavioral assays (Fig. 2A, a) solitary, b) social and c) fear). This pre-screening step reinforced the expression of social behaviors (*11, 12*), and the display of fear behaviors during the recording sessions (Fig. S3). Following the probe implantation, animals were allowed to recover and were habituated to the experimental setup in the absence of the behavioral assays (Fig. 2B).

As previous work has shown that the neural firing rates often correlate with motion-related variables in some brain areas (*31-33*), we assessed this question in our mesoscale hypothalamic recordings. Self-motion variables and distance between animals did not correlate with mean single unit firing rates, either during whole recording sessions (Fig. S4, A and B), or during specific behavior actions (Fig. S5, A-D). Partial least squares (PLS) regression (Fig. S5, E-G) provided further evidence that single unit activity also does not correlate with motion variables (Fig. S5Ed). However, the PLS regression revealed that single-unit activity was correlated with consummatory and, to a lesser extent, appetitive social and fear behaviors (Fig. S5, Fd and Gd).

130 **Spatially distributed and behavior non-specific neural "ignition signals"**

131 Next, we sought to address whether activity during specific appetitive and consummatory behaviors,
132 including intermale social behaviors (Fig. 2, C and D), male-female social behaviors (Fig. 2, E and F),
133 and predatory defensive behaviors (Fig. 2, G and H), is restricted anatomically or rather spatially
134 distributed, based on averaging units recorded from each of the twenty nuclei. Throughout the entire
135 hypothalamus we observed a synchronous burst of activity near the onset of all behaviors except for
136 predator-induced freezing (Fig. 2, C-G). This spiking burst that occurred at all behavior onsets following
137 the introduction of an intruder (example behavior raster plot shown in Fig. S6A) appeared consistently
138 across behavioral episodes (Fig. S6, B and C). It had an onset of -200 msec prior to the initiation of
139 behavior (Fig. S6E), average duration of 1.5 sec (Fig. S6F), and always ended before the termination of
140 the behavior (Fig. S6G). This response, which we refer to here as an "ignition signal," encompassed ~25-
141 35% of recorded units across the entire hypothalamus, except for freezing behavior which engaged only
142 7% of units (Fig. 2D-H, gray/black pie charts). The ignition signal was observed across multiple episodes
143 of a given behavior directed towards the same intruder or predator (Fig. S4, C and D, and Fig. S6, A-C),
144 indicating that it did not simply represent a novelty or neophobic response. However, the activity levels
145 and proportion of the neurons recruited across behaviors markedly differed across nuclei (Fig. 2, C, E
146 and G – right bar plots). Each nucleus was differentially activated during behaviors of interest (Fig. 2, D,
147 F and H). Together, these findings indicate that ignition signals, while globally distributed, exhibit
148 quantitative biases in their anatomic distribution that likely reflect behavior-specific responses in different
149 hypothalamic nuclei (Fig. 2, D, F and H).

150 The near-uniform expression of ignition signals likely accounts for the lack of statistical significance
151 in decoding behaviors from nucleus-averaged neural activity (SVM decoding models, Fig. S4E). An
152 analysis of activity at single-unit resolution – discussed in the next section, however, could help to address
153 whether behavior-specific modes of activity exist at the level of individual neurons.

154

155 **Single neuron activity primarily encodes distinct behavior classes**

156 To investigate the representation of behavior by single neurons in the hypothalamus, we annotated
157 43 behavioral actions among the different classes and domains (functional models discussed in Fig. 1I,
158 right). Using these annotations, the first approach we used was to compute the single neuron activity-
159 based behavior correlation matrix (Fig. 3, Aa-Ad). Using rastermap(*34*), we sorted the row and column
160 indices of the behavior correlation matrix to maximize similarity between consecutive rows and columns,
161 which allowed us to visually evaluate the differences in neural representations across behaviors (Fig.
162 3B). Following averaging of the behavior correlation matrix across six mice, we observed a prominent
163 segregation between social and predatory-defensive behavioral classes (note the separation of red-
164 ["fear"] vs. green- and purple-tagged [social] behaviors in Fig. 3B). This effect was also prominent in the
165 behavior correlation matrices of individual mice (Fig. S7, except for mouse #4). Overall, this analysis
166 revealed that social and fear behavioral classes can be broadly segregated based on neuron population
167 activity. Male- and female-directed social behaviors were also generally separated, but not as
168 prominently. Related individual actions had correlated neural patterns to some extent within domains
169 (Fig. 3B, sorting of behavior actions reflects similarity in their encoding).

170 The results of the behavior correlation matrix suggested that social and fear behaviors are encoded
171 differently by hypothalamic neurons. However, this population-level analysis cannot distinguish whether
172 individual behaviors are encoded by the same set of neurons that exhibit behavior class-specific activity
173 patterns or whether distinct groups of neurons encode distinct behavior classes. To address this question,
174 we next used a more targeted method, focusing on only two representative behavioral actions from each
175 of the four behavioral domains of interest (total of eight behavioral actions, Fig. 3C). This approach could
176 1) confirm or disprove the segregation of social vs. fear behaviors, and 2) if the former is the case, indicate
177 whether this segregation reflects different neuron groups active in the two behavioral classes, or whether
178 it is driven by different patterns of activity exhibited by the same neurons.

179 In the solitary domain, the self-grooming (sg) and rearing (r) behavioral actions were included.
180 Representative behavioral actions in the intermale domain were male intruder sniffing (ms), and attack

181 (ma), while in the male-female domain female intruder sniffing (fs) and mounting (fm) were included.
182 Lastly, in the predatory fear domain, the rat sniffing (rs) and escape response (re) behavior actions were
183 included. The timepoints of three episodes per behavior were extracted from the experimental design
184 illustrated in Fig. 3Aa. Specifically, solitary behavior episodes were extracted from experiment (a),
185 female-oriented behavior episodes were extracted from experiments (a) and (b), male-oriented behavior
186 episodes were extracted from experiments (c) and (d), and predator-defence behavior episodes were
187 extracted from experiment (e). Fig. S8A shows the activity of single units across the eight above-
188 mentioned behavioral actions, across three consecutive behavioral episodes. The activity of single units
189 was sorted from high to low within each brain area.

190 To test whether separate groups of recorded units exhibit distinct behavior-correlated activity profiles,
191 we performed *k*-means clustering of the single neuron activity (single neuron activity is shown in Fig.
192 S8A). The number of clusters, 41, was selected using the elbow method (*35, 36*); 41 clusters explained
193 70% of the single neuron activity data variance. The average activity of each of the 41 clusters during the
194 8 different domain-specific actions was plotted for each of the three consecutive episodes (Fig. 3C).
195 Agglomerative hierarchical linkage clustering (ALC) of these 41 clusters revealed five groups (i.e.,
196 dendrogram branches, Fig. 3C, right, threshold for separating branches of the dendrogram was defined
197 using the elbow method). This analysis suggested that the social and fear behavior classes are encoded
198 by functionally distinct groups of hypothalamic neurons (Fig. 3C, highlighted as blue [social] and red
199 [predatory fear] clusters in the dendrogram). This finding was also qualitatively supported by performing
200 non-negative matrix factorization (NMF) on the data shown in Fig. S8A. However, with NMF, the
201 distinction between social- vs. fear-correlated ensemble activity was less prominent (Fig. S9, A and B).
202 The weaker segregation of behavioral classes through NMF likely reflects that NMF allows neurons to
203 contribute to multiple factors (components).

204 While the *k*-means clusters associated with social or fear behavior classes were well separated,
205 neurons exhibited multi-action activity, also known as mixed selectivity, within each class-specific cluster.
206 To quantify this finding, we classified a cluster as active during a specific action if its activity (spiking rate)

207 was ≥ 2σ above its baseline activity. Accordingly, 56% of all clusters were identified to exhibit mixed
208 selectivity within their respective behavior classes. Only seven percent of hypothalamic clusters exhibited
209 mixed selectivity within a single behavioral domain (male- or female-directed behavior; Fig. 3E), while
210 27% of clusters showed prominent activity during only a single action (Fig. 3F). While the activity of any
211 single cluster exhibited adaptation across episodes (Fig. S8B) there was an overall positive correlation
212 between episodes (Fig. S8C) and a high-fidelity score (a measure of a cluster being identified as active
213 in the same behavior(s) across episodes, Fig. S8D). Thus, the representation of behavioral actions by
214 different clusters is reproducible across episodes, but not rigidly fixed.
215

216 **Encoding of behavior is spatially distributed, but individual ensembles are**
217 **anatomically clustered**

218 The foregoing analysis revealed that distinct neuron clusters encode social and fear behavior classes.
219 We next sought to determine whether individual activity-defined ensembles are anatomically localized
220 and whether they respect classical cytoarchitectonically defined nuclear boundaries.

221 We found that a) functionally similar clusters were distributed broadly across the hypothalamic rostro-
222 caudal axis (Fig 4A), and b) that most clusters were composed of cells that originated from a few
223 neighboring hypothalamic regions (Fig. 4B). Re-sorting these clusters within each branch of the
224 dendrogram according to their position along the rostro-caudal axis (Fig. 4C), revealed that each behavior
225 class was broadly represented along this axis (Fig. 4C).

226 The number of regions contributing to single clusters was typically four areas (Fig. 4d), suggesting
227 that most hypothalamic clusters consist of cells that originate from four neighbouring hypothalamic
228 regions. The same observation occurred when quantifying the composition of clusters that were identified
229 as “social”, female-specific, and predatory-fear relevant (Fig. 4D – inset). We investigated whether
230 increasing the number of clusters in *k*-means leads to a reduced number of regions per cluster (Fig. 4E).
231 However, we found an asymptote at an average number of four nuclei per cluster which did not further

232 decrease even when the number of clusters was increased up to 120 (Fig. 4E). The smallest number of
233 clusters that reached the asymptotic value of 4 regions per cluster was 41, and this model explained a
234 majority of the variance in the data (70%). A qualitatively similar result emerged when analyzing factors
235 identified by NMF, with closely related factors composed of neurons at different positions along the rostro-
236 caudal axis, and heavily weighted neurons in each factor were present in neighboring hypothalamic
237 regions (Fig. S9, D and E).
238

239 **Behavior explains a quarter of the variance of hypothalamic neuron activity**

240 The above approaches suggest that: 1) distinct populations of neurons represent social and fear
241 behaviors, 2) the encoding of each behavioral class is represented by a set of clusters comprised of units
242 defined by correlated neuronal activity, which are spatially distributed across the rostro-caudal axis, and
243 3) individual clusters typically contained neurons from ca. four neighboring nuclei, therefore exhibiting a
244 strong local anatomical bias in their composition. However, since most of the units in these functional
245 clusters exhibited mixed selectivity, it remained uncertain whether specific behavior actions could be
246 decoded from neural activity.

247 To determine whether individual behavioral actions could be predicted from single-unit activity, we
248 trained decoders based on neural activity using two different machine learning algorithms (gradient
249 boosted trees (*37*), results plotted in Fig. S10, and support vector machines (*23*), results plotted in Fig.
250 S11). A subset of appetitive and consummatory representative behavior actions per behavioral domain
251 were selected to address the above point. The results indicated that most, but not all, actions within each
252 of the four different behavioral domains could be decoded from neural data significantly better than
253 chance. In the case of male-directed attack, decoder performance was high, reaching a shuffled
254 subtracted median F1 score of ~0.5 (Fig. S10B).

255 The foregoing analysis suggested that behavioral actions could be decoded from neural activity but
256 left open the question of which features of these behaviors were encoded. To address this question, we

257 next examined how well the firing patterns of individual units could be predicted from a weighted sum of
258 different behavioral actions and features (features included animal's velocity, acceleration, distance, and
259 angle between animals). These features were computed based on pose estimation using DeepLabCut
260 (*38*).

261 For this purpose, we trained generalized linear models (GLMs) (*39, 40*) to predict the activity of each
262 neuron based on a weighted sum of selected predictor variables (design of GLMs shown in Fig. 5A). This
263 approach can: 1) identify the overall variance explained by specific predictors (Fig. 5B), 2) reveal the
264 influence of all annotated predictors on single neuron activity, by inspection of their coefficients/weights
265 (Fig. 5C), and 3) indicate whether neurons that belong to the same cluster (based on the similarity of their
266 behavior weights – Fig. 5C, see dendrogram colored branches) show any spatial bias (Fig. 5, D and E).

267 First, we sought to identify the percentage of variance explained by the four high-level behavior
268 classes. Only 8% of the variance of single neuron activity was accounted for by the four behavioral
269 domains (Fig. S12A). Next, we examined the percent of variance explained by forty behavioral actions,
270 annotated across the four behavioral domains of interest. Behavioral actions alone explained 23% of the
271 variance of hypothalamic neuron activity ($R^2$ median = 0.23, Fig. 5B). Training GLM models with predictor
272 variables being the behavioral actions, plus motion signals (the animals' velocity and acceleration), and
273 proxies of sensory cues (distance and angle between animals), did not lead to an increase in the variance
274 explained (Fig. S12, C-E).

275 Many different behaviors had positive and negative weights on the activity pattern of each single-unit
276 (Fig. 5C), highlighting mixed selectivity as a prime mode of the hypothalamic encoding of behavior, and
277 providing further support to the results of the *k*-means (Fig. 3D) and NMF analysis (Fig. S9A). Application
278 of agglomerative clustering (ALC) to the matrix of GLM-derived behavior weights yielded 24 clusters of
279 neurons (the elbow method was used to select the number of clusters). Each cluster (Fig. 5C) contained
280 a unique combination of neurons whose activity was influenced by a specific set of behavior weights (Fig.
281 5C), with a near-uniform contribution of neurons from each of the six recorded mice (Fig. S13A). Sorting
282 these neurons based on their relative spatial location, however, did not generate clusters in a pattern

similar to that identified by ALC, suggesting that the neurons comprising the clusters are not restricted to single hypothalamic nuclei (Fig. S13B). To investigate whether the cells comprising the ALC-generated neuron clusters exhibit any restriction in their anatomic distribution, we measured the average contribution of each nucleus to each cluster (Fig. 5D, rows). This revealed that clusters indeed exhibited a spatial bias, with >80% of the cells comprising each cluster originating from ~four nearby regions (Fig. 5, D and E) – a finding consistent with the *k*-means-revealed cluster spatial bias (Fig. 4D). Also similar to the *k*-means analysis, we found that GLM-based clusters exhibited spatial bias and mixed selectivity (Fig. 3D and 4C), which we quantified using a spatial localization index (single nucleus restricted vs. broadly distributed) and using encoding entropy respectively (the degree of behavior specific vs. mixed selectivity coding; see Materials and Methods section: GLM output – functional vs. spatial distribution of clusters).

## Discussion

The hypothalamus is traditionally viewed as a "low-dimensional" system in which innate social, defensive, and feeding behaviors are controlled by bulk neural activity flowing through specific pathways connecting functionally specialized anatomical subdivisions and cell types (*41-43*). In contrast, the cortico-hippocampal system is thought to operate using high-dimensional, dynamic neural codes involving complex spatio-temporal patterns of population activity (*44-47*). Here, we addressed whether this difference is truly biological or reflects the fact that most recording studies in the hypothalamus have used low-dimensional recording methods (e.g., fiber photometry) applied to anatomically restricted regions pre-selected based on perturbational studies. We report here what is, to our knowledge, the first unbiased high-dimensional single-unit recording of neural activity along the rostro-caudal axis of the medial hypothalamus during social and predator-defense behaviors. Our results suggest that behavioral coding in the hypothalamus is more high-dimensional, spatially distributed, dynamic, and variable than previously appreciated.

Several unexpected findings have emerged from this study. First, we observe that the initiation of these innate behaviors is (except for freezing) preceded by a hypothalamus-wide, synchronous burst of peri-onset activity, which we call an "ignition signal." Second, we find that functionally distinct subpopulations of neurons (defined by unbiased *k*-means clustering) encode social (mating and fighting) vs. predator defense behavioral classes. Specific behavioral actions or male- vs. female-directed social behaviors are less well-discriminated by such clusters. While these clusters are reproducibly activated across multiple episodes of each behavioral class, inter-episodic variability exists in the recruitment and activity level of the neurons comprising each cluster. Nevertheless, despite this variability, many behavioral actions could be decoded from single-unit activity with high accuracy. Third, we find that the subpopulations representing social and defense behaviors are broadly distributed across the rostro-caudal length of the hypothalamus rather than spatially localized to a single nucleus or region. Fourth, we find that cluster membership draws from neurons distributed in neighboring nuclei, typically four.

318 Nevertheless, behavior cannot be decoded from bulk neural activity based on anatomical location alone.
319 Finally, we find that a substantial fraction (median 23%) of the single-neuron variance in activity can be
320 explained by behavioral actions and, to a lesser degree, by behavioral domains. We consider the median
321 $R^2$ of 0.23 as a high value, as other studies which used brain wide recordings during stereotyped
322 behavioral tasks in head-fixed mice reported a cross-validated variance explained in single neuron
323 activity in the range of 5-15% (*48, 49*).

324 The present study paints an overall picture that challenges prevailing views of behavioral encoding
325 by the hypothalamus. We note that if these data had provided the very first, foundational view of
326 hypothalamic behavioral encoding, they would not have directed subsequent functional perturbations to
327 specific single nuclei such as VMH (*11, 13, 22, 23, 50-55*) or MPOA (*14, 56-60*). Instead, they would
328 have prompted the study of behavior encoding units across several neighboring nuclei. They would have
329 shifted the focus from seeking the identification of behavior-specific cell types to understanding the
330 properties conferred by the prime mode of activity we report here, i.e., mixed selectivity (*61-65*).

331 Is there any way to reconcile these two seemingly opposing views of behavioral control by the
332 hypothalamus? There are several possible explanations. One possibility is that prior, low-dimensional,
333 anatomically restricted approaches have missed what is suggested by our silicon probe recordings: i.e.,
334 that the "units" of hypothalamic computations are anatomically distributed, and that mixed-selectivity is
335 the prime mode of hypothalamic behavioral encoding. Recent studies suggest that even in the absence
336 of behavior action-tuned cells, behavior can still be decoded with high accuracy, with mixed selectivity
337 providing a basis for the encoding of numerous and diverse features in a computationally efficient manner
338 (*61-64*). For example, non-linear mixed selectivity enables the integration of diverse lines of information
339 in single neurons that can elicit behavior actions based on a threshold mechanism.

340 A second possibility is that our silicon probe recordings have missed anatomically restricted behavior-
341 specific subsets. This could be due to sparse sampling (we recorded on average only ~20 units per
342 nucleus per animal) and/or to variability in the activity of individual units across episodes and animals

343 during a given behavior, perhaps reflecting representational drift (*66, 67*) or stochastic recruitment of
344 individual units (*68*). This variability may explain, in part, why a recent multi-site coarse recording of bulk
345 calcium activity from Esr1$^+$ neurons across the hypothalamus yielded reproducible, spatially distinct
346 patterns of activity during male- vs. female-directed social behaviors, in specific nuclei previously
347 identified as causally relevant to these behaviors by perturbation studies (*69*). Alternatively, Esr1$^+$
348 neurons may represent a "privileged," more behavior-specific subpopulation than the "anonymous" units
349 sampled here. A third possibility (not mutually exclusive with the second) is that the intrinsic variability in
350 the performance or sequence of specific behavioral actions during a given activity (e.g., a male-male
351 social interaction) may confound efforts to correlate a high-granularity annotation of these actions (43)
352 with high-dimensional neural data (~2400 units from 6 animals). Finally, we note that causation and
353 representation are not the same thing: not all neural representations during a given behavior necessarily
354 reflect a causal role for those neurons; for example, some activated units may represent efference copies
355 of motor signals, or GABAergic neurons that serve to inhibit competing behaviors.

356 Further work is required to distinguish these possibilities and to arrive at an understanding of
357 behavioral coding and function that reconciles and integrates the two views of hypothalamic computations
358 provided by recording and perturbation strategies, respectively. At the very least, our data indicate that
359 the application to the hypothalamus of unbiased, large-scale, anonymous single-unit recordings reveals
360 a surprisingly complex pattern of spatio-temporal activity that does not easily map to specific nuclei or
361 single behavior actions. It suggests that the prevailing view of the hypothalamus as a low-dimensional
362 control system needs to be revised, or alternatively that the signals that control behavior are, to a large
363 extent, "hidden" in the population code.

# References


1. X. D. Lin *et al.*, High-throughput mapping of brain-wide activity in awake and drug-responsive vertebrates. *Lab on a chip* **15**, 680-689 (2015).
2. E. Litvina *et al.*, BRAIN Initiative: Cutting-Edge Tools and Resources for the Community. *Journal of Neuroscience* **39**, 8275-8284 (2019).
3. M. G. Perich, K. Rajan, Rethinking brain-wide interactions through multi-region 'network of networks' models. *Current opinion in neurobiology* **65**, 146-151 (2020).
4. B. J. Edelman, E. Macé, Functional ultrasound brain imaging: Bridging networks, neurons, and behavior. *Current Opinion in Biomedical Engineering* **18**, (2021).
5. T. Schrodel, R. Prevedel, K. Aumayr, M. Zimmer, A. Vaziri, Brain-wide 3D imaging of neuronal activity in Caenorhabditis elegans with sculpted light. *Nature methods* **10**, 1013-1020 (2013).
6. S. Brodt *et al.*, Fast track to the neocortex: A memory engram in the posterior parietal cortex. *Science* **362**, 1045-+ (2018).
7. F. Chersi, N. Burgess, The Cognitive Architecture of Spatial Navigation: Hippocampal and Striatal Contributions. *Neuron* **88**, 64-77 (2015).
8. C. F. Doeller, C. Barry, N. Burgess, Evidence for grid cells in a human memory network. *Nature* **463**, 657-U687 (2010).
9. S. F. Grieco, T. C. Holmes, X. M. Xu, Probing neural circuit mechanisms in Alzheimer's disease using novel technologies. *Mol Psychiatr*, (2023).
10. D. F. Tomé, S. Sadeh, C. Clopath, Coordinated hippocampal-thalamic-cortical communication crucial for engram dynamics underneath systems consolidation. *Nature communications* **13**, (2022).
11. S. Stagkourakis, G. Spigolon, G. Liu, D. J. Anderson, Experience-dependent plasticity in an innate social behavior is mediated by hypothalamic LTP. *Proceedings of the National Academy of Sciences of the United States of America* **117**, 25789-25799 (2020).
12. S. Stagkourakis *et al.*, A neural network for intermale aggression to establish social hierarchy. *Nature neuroscience* **21**, 834-+ (2018).
13. D. Lin *et al.*, Functional identification of an aggression locus in the mouse hypothalamus. *Nature* **470**, 221-226 (2011).
14. T. Karigo *et al.*, Distinct hypothalamic control of same- and opposite-sex mounting behaviour in mice (vol 589, pg 258, 2021). *Nature* **589**, E9-E9 (2021).
15. P. S. Kunwar *et al.*, Ventromedial hypothalamic neurons control a defensive emotion state. *eLife* **4**, (2015).
16. A. Adhikari *et al.*, Basomedial amygdala mediates top-down control of anxiety and fear. *Nature* **527**, 179-+ (2015).
17. J. Kim, X. Y. Zhang, S. Muralidhar, S. A. LeBlanc, S. Tonegawa, Basolateral to Central Amygdala Neural Circuits for Appetitive Behaviors. *Neuron* **93**, 1464-+ (2017).
18. N. Scott, M. Prigge, O. Yizhar, T. Kimchi, A sexually dimorphic hypothalamic circuit controls maternal care and oxytocin secretion. *Nature* **525**, 519-+ (2015).
19. S. Stagkourakis, G. Spigolon, G. Liu, D. J. Anderson, Experience-dependent plasticity in an innate social behavior is mediated by hypothalamic LTP. *Proceedings of the National Academy of Sciences of the United States of America* **117**, 25789-25799 (2020).
20. D. Mahadevia *et al.*, Dopamine promotes aggression in mice via ventral tegmental area to lateral septum projections. *Nature communications* **12**, (2021).
21. A. L. Falkner *et al.*, Hierarchical Representations of Aggression in a Hypothalamic-Midbrain Circuit. *Neuron* **106**, 637-648 e636 (2020).
22. H. Lee *et al.*, Scalable control of mounting and attack by Esr1+ neurons in the ventromedial hypothalamus. *Nature* **509**, 627-632 (2014).

23. R. Remedios *et al.*, Social behaviour shapes hypothalamic neural ensemble representations of conspecific sex. *Nature* **550**, 388-+ (2017).
24. A. Nair *et al.*, An approximate line attractor in the hypothalamus encodes an aggressive state. *Cell* **186**, 178-193 e115 (2023).
25. A. Asaba *et al.*, Prelimbic cortex responds to male ultrasonic vocalizations in the presence of a male pheromone in female mice. *Frontiers in neural circuits* **16**, (2022).
26. K. K. Ishii, K. Touhara, Neural circuits regulating sexual behaviors via the olfactory system in mice. *Neuroscience research* **140**, 59-76 (2019).
27. T. Itakura *et al.*, A single vomeronasal receptor promotes intermale aggression through dedicated hypothalamic neurons. *Neuron* **110**, 2455-2469 e2458 (2022).
28. N. Renier *et al.*, iDISCO: A Simple, RapidMethod to Immunolabel Large Tissue Samples for Volume Imaging. *Cell* **159**, 896-910 (2014).
29. Q. X. Wang *et al.*, The Allen Mouse Brain Common Coordinate Framework: A 3D Reference Atlas. *Cell* **181**, 936-+ (2020).
30. N. A. Steinmetz *et al.*, Neuropixels 2.0: A miniaturized high-density probe for stable, long-term brain recordings. *Science* **372**, 258-+ (2021).
31. M. Vinck, R. Batista-Brito, U. Knoblich, J. A. Cardin, Arousal and Locomotion Make Distinct Contributions to Cortical Activity Patterns and Visual Encoding. *Neuron* **86**, 740-754 (2015).
32. M. C. Dadarlat, M. P. Stryker, Locomotion Enhances Neural Encoding of Visual Stimuli in Mouse V1. *Journal of Neuroscience* **37**, 3764-3775 (2017).
33. A. J. Christensen, J. W. Pillow, Reduced neural activity but improved coding in rodent higher-order visual cortex during locomotion. *Nature communications* **13**, 1676 (2022).
34. Z. L. Stringer C., Syeda A., Du F., Kesa M., & Pachitariu M., Rastermap: a discovery method for neural population recordings. *bioRxiv*, (2023).
35. C. Goutte, P. Toft, E. Rostrup, F. Å. Nielsen, L. K. Hansen, On clustering fMRI time series. *NeuroImage* **9**, 298-310 (1999).
36. R. L. Thorndike, Who Belongs in the Family? *Psychometrika* **18**, 267-276 (1953).
37. G. Viejo, T. Cortier, A. Peyrache, Brain-state invariant thalamo-cortical coordination revealed by non-linear encoders. *PLoS computational biology* **14**, (2018).
38. A. Mathis *et al.*, DeepLabCut: markerless pose estimation of user-defined body parts with deep learning. *Nature neuroscience* **21**, 1281-1289 (2018).
39. A. I. Weber, J. W. Pillow, Capturing the Dynamical Repertoire of Single Neurons with Generalized Linear Models. *Neural computation* **29**, 3260-3289 (2017).
40. I. M. Park, M. L. R. Meister, A. C. Huk, J. W. Pillow, Encoding and decoding in parietal cortex during sensorimotor decision-making. *Nature neuroscience* **17**, 1395-1403 (2014).
41. L. Mei, T. Osakada, D. Lin, Hypothalamic control of innate social behaviors. *Science* **382**, 399-404 (2023).
42. J. D. Hahn, G. Fink, M. R. Kruk, B. G. Stanley, Editorial: Current Views of Hypothalamic Contributions to the Control of Motivated Behaviors. *Frontiers in systems neuroscience* **13**, (2019).
43. C. Dulac, L. A. O'Connell, Z. Wu, Neural control of maternal and paternal behaviors. *Science* **345**, 765-770 (2014).
44. J. Basu, S. A. Siegelbaum, The Corticohippocampal Circuit, Synaptic Plasticity, and Memory. *Cold Spring Harb Perspect Biol* **7**, (2015).
45. M. C. Aoi, V. Mante, J. W. Pillow, Prefrontal cortex exhibits multidimensional dynamic encoding during decision-making. *Nature neuroscience* **23**, 1410-1420 (2020).
46. A. Sarel *et al.*, Natural switches in behaviour rapidly modulate hippocampal coding. *Nature* **609**, 119-127 (2022).
47. J. Kim, A. Joshi, L. Frank, K. Ganguly, Cortical-hippocampal coupling during manifold exploration in motor cortex. *Nature* **613**, 103-110 (2023).

48. N. A. Steinmetz, P. Zatka-Haas, M. Carandini, K. D. Harris, Distributed coding of choice, action and engagement across the mouse brain. *Nature* **576**, 266-+ (2019).
49. W. E. Allen *et al.*, Thirst regulates motivated behavior through modulation of brainwide neural population dynamics. *Science* **364**, 253-+ (2019).
50. A. Kennedy *et al.*, Stimulus-specific hypothalamic encoding of a persistent defensive state. *Nature* **586**, 730-734 (2020).
51. T. Yang *et al.*, Social Control of Hypothalamus-Mediated Male Aggression. *Neuron* **95**, 955-+ (2017).
52. K. K. Ishii *et al.*, A Labeled-Line Neural Circuit for Pheromone-Mediated Sexual Behaviors in Mice. *Neuron* **95**, 123-+ (2017).
53. A. L. Falkner, L. Grosenick, T. J. Davidson, K. Deisseroth, D. Y. Lin, Hypothalamic control of male aggression-seeking behavior. *Nature neuroscience* **19**, 596-+ (2016).
54. H. Lee *et al.*, Scalable control of mounting and attack by Esr1<SUP>+</SUP> neurons in the ventromedial hypothalamus. *Nature* **509**, 627-+ (2014).
55. C. F. Yang *et al.*, Sexually Dimorphic Neurons in the Ventromedial Hypothalamus Govern Mating in Both Sexes and Aggression in Males. *Cell* **153**, 896-909 (2013).
56. D. Liu *et al.*, A Hypothalamic Circuit Underlying the Dynamic Control of Social Homeostasis. *bioRxiv*, (2023).
57. S. Stagkourakis *et al.*, A Neuro-hormonal Circuit for Paternal Behavior Controlled by a Hypothalamic Network Oscillation. *Cell* **182**, 960-+ (2020).
58. L. Mei, R. Z. Yan, L. P. Yin, R. M. Sullivan, D. Y. Lin, Antagonistic circuits mediating infanticide and maternal care in female mice. *Nature*, (2023).
59. S. X. Zhang *et al.*, Hypothalamic dopamine neurons motivate mating through persistent cAMP signalling. *Nature* **597**, 245-+ (2021).
60. J. Kohl, C. Dulac, Neural control of parental behaviors. *Current opinion in neurobiology* **49**, 116-122 (2018).
61. S. Kira, H. Safaai, A. S. Morcos, S. Panzeri, C. D. Harvey, A distributed and efficient population code of mixed selectivity neurons for flexible navigation decisions. *Nature communications* **14**, 2121 (2023).
62. M. T. Kaufman *et al.*, The implications of categorical and category-free mixed selectivity on representational geometries. *Current opinion in neurobiology* **77**, 102644 (2022).
63. W. J. Johnston, S. E. Palmer, D. J. Freedman, Nonlinear mixed selectivity supports reliable neural computation. *PLoS computational biology* **16**, e1007544 (2020).
64. I. S. Grunfeld, E. Likhtik, Mixed selectivity encoding and action selection in the prefrontal cortex during threat assessment. *Current opinion in neurobiology* **49**, 108-115 (2018).
65. M. Rigotti *et al.*, The importance of mixed selectivity in complex cognitive tasks. *Nature* **497**, 585-590 (2013).
66. C. E. Schoonover, S. N. Ohashi, R. Axel, A. J. P. Fink, Representational drift in primary olfactory cortex. *Nature* **594**, 541-546 (2021).
67. P. Zhao *et al.*, Accelerated social representational drift in the nucleus accumbens in a model of autism. *bioRxiv*, (2023).
68. C. Haimerl, C. Savin, E. P. Simoncelli, Flexible information routing in neural populations through stochastic comodulation. *Advances in Neural Information Processing Systems 32 (Nips 2019)* **32**, (2019).
69. Z. Guo *et al.*, Neural dynamics in the limbic system during male social behaviors. *Neuron*, (2023).
70. C. Segalin *et al.*, The Mouse Action Recognition System (MARS) software pipeline for automated analysis of social behaviors in mice. *eLife* **10**, (2021).
71. J. J. Jun *et al.*, Fully integrated silicon probes for high-density recording of neural activity. *Nature* **551**, 232-+ (2017).
72. S. M. Lundberg, S. I. Lee, A Unified Approach to Interpreting Model Predictions. *Adv Neur In* **30**, (2017).
73. T. Q. Chen, C. Guestrin, XGBoost: A Scalable Tree Boosting System. *Kdd'16: Proceedings of the 22nd Acm Sigkdd International Conference on Knowledge Discovery and Data Mining*, 785-794 (2016).

506 **Acknowledgments**

507 Members of the Anderson laboratory are thanked for their advice and discussion during the preparation
508 of this manuscript. Light-sheet imaging was performed in the Biological Imaging Facility, with the support
509 of the Caltech Beckman Institute and the Arnold and Mabel Beckman Foundation. Special thanks to the
510 Director of the Biological Imaging Facility at Caltech, Dr. Andres Collazo, for providing crucial
511 experimental support and advice. We also thank Jung-Sook Chang and Xiaolin Da for experimental
512 support, C. Chiu for laboratory management, G. Mancuso, L. Chavarria and D. R. Navarrete for
513 administrative assistance. S.S. received support from the Wenner-Gren Foundations and by NIH
514 K99MH131754. D.J.A. is an investigator of the Howard Hughes Medical Institute. This work was
515 supported in part by NIH grants NS123916, MH1223612, and MH070053 to D.J.A. The content is solely
516 the responsibility of the authors and does not necessarily represent the official views of the National
517 Institutes of Health. All authors support an inclusive, diverse, and equitable conduct of research.

518

519

520 **Author contributions**

521 S.S. conceived the study, designed and performed all experiments, wrote hardware-operating and
522 analysis code, analyzed data, and generated the first draft of the manuscript. G.S. contributed to brain
523 clearing, light-sheet microscopy, and silicon probe registration to the Allen Common Coordinate
524 Framework. M.M. performed the decoding analysis using gradient boosted trees. P.P. designed decoding
525 approaches. M.F. wrote and provided code for image registration for light-sheet microscopy data. J.K.
526 contributed to the analysis. M.P. supervised S.S.. D.J.A. supervised S.S., contributed to the study design
527 and analysis, and wrote the manuscript. All authors reviewed the manuscript.

528

529

530 **Competing interests**

531 The authors declare no competing financial interests.

# Main Figures

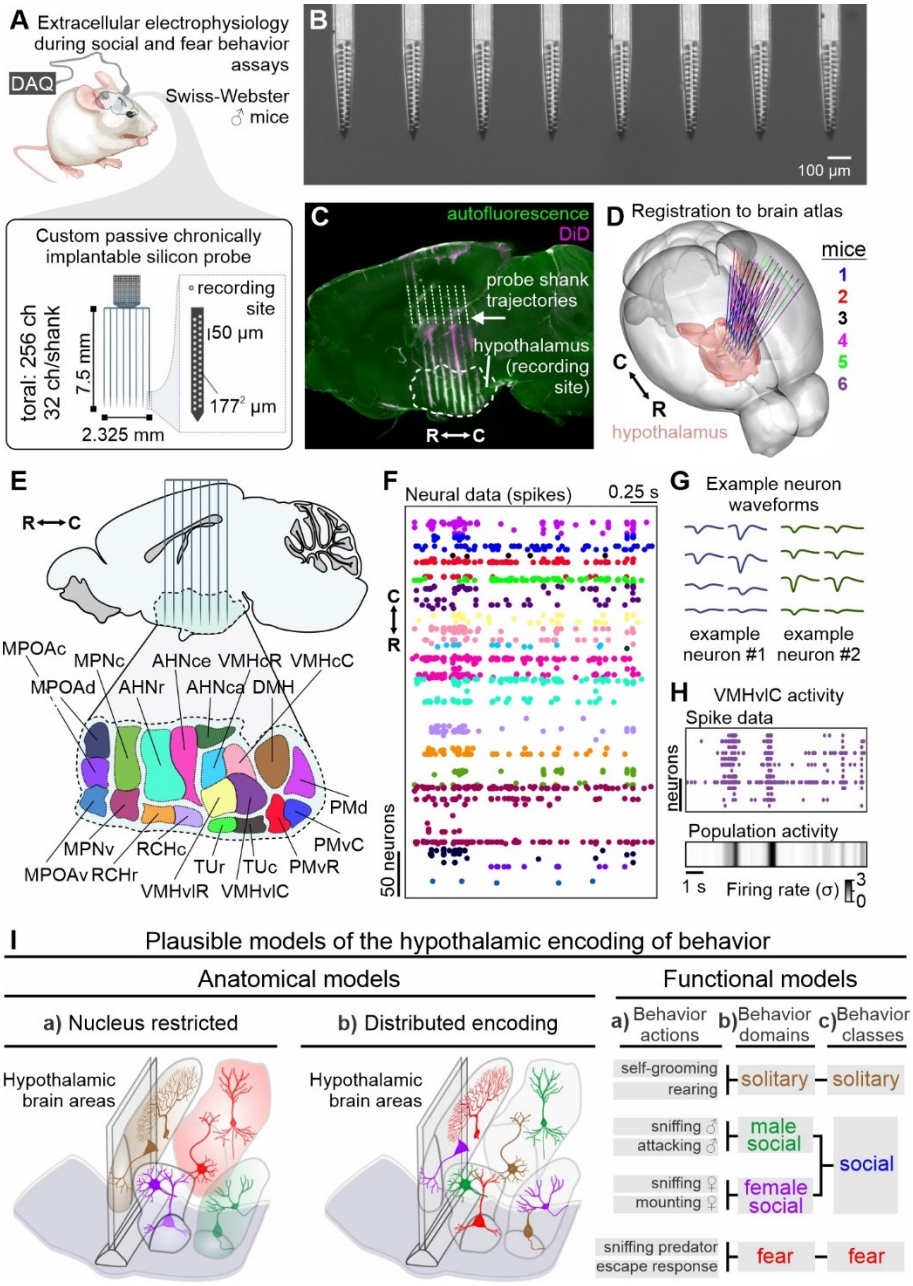


**Fig. 1. Approach for single neuron recordings across the hypothalamus using custom extracellular electrophysiology silicon probes in freely moving mice.** (**A**) Top - outbred Swiss Webster male mice were chronically implanted with a custom silicon probe. Bottom - design, and specifics of the eight-shank 256-channel custom silicon probe manufactured by NeuroNexus. (**B**) Stereoscope-acquired image of the shank-tips of the probe containing the microelectrodes. (**C**) Post-hoc identification of probe shanks and electrode placement through volumetric light-sheet imaging. (**D**) Registration of the

probes to the Allen Common Coordinate Framework across all recorded mice. (**E**) Target coordinates include twenty, individually colored subregions of the hypothalamus. (**F**) Following electrode mapping and spike sorting, single neurons were assigned to their respective locations / hypothalamic areas. (**G**) Example waveforms of two recorded neurons. (**H**) Example spike data across thirteen neurons of VMHvl (top), and illustration of their average activity (bottom). (**I**) Spatial and functional plausible models, combination of which could explain the hypothalamic encoding of behavior.

Abbreviations: DAQ: data acquisition system, MPOAv: medial preoptic area – ventral subdivision. MPOAc: medial preoptic area – central subdivision. MPOAd: medial preoptic area – dorsal subdivision. MPNv: medial preoptic nucleus – ventral subdivision. MPNc: medial preoptic nucleus – central subdivision. RCHr: retrochiasmatic area – rostral subdivision. RCHc: retrochiasmatic area – caudal subdivision. AHNr: anterior hypothalamic nucleus – rostral subdivision. AHNce: anterior hypothalamic nucleus – central subdivision. AHNca: anterior hypothalamic nucleus – caudal subdivision. TUr: tuberal nucleus – rostral subdivision. TUc: tuberal nucleus – caudal subdivision. VMHvlR: ventromedial hypothalamic nucleus ventrolateral segment – rostral subdivision. VMHvlC: ventromedial hypothalamic nucleus ventrolateral segment – caudal subdivision. VMHcR: ventromedial hypothalamic nucleus central segment – rostral subdivision. VMHcC: ventromedial hypothalamic nucleus central segment – caudal subdivision. DMH: dorsomedial hypothalamic nucleus. PMvR: ventral premammillary nucleus – rostral subdivision. PMvC: ventral premammillary nucleus – caudal subdivision. PMd: dorsal premammillary nucleus. See also Fig. S1 and S2.

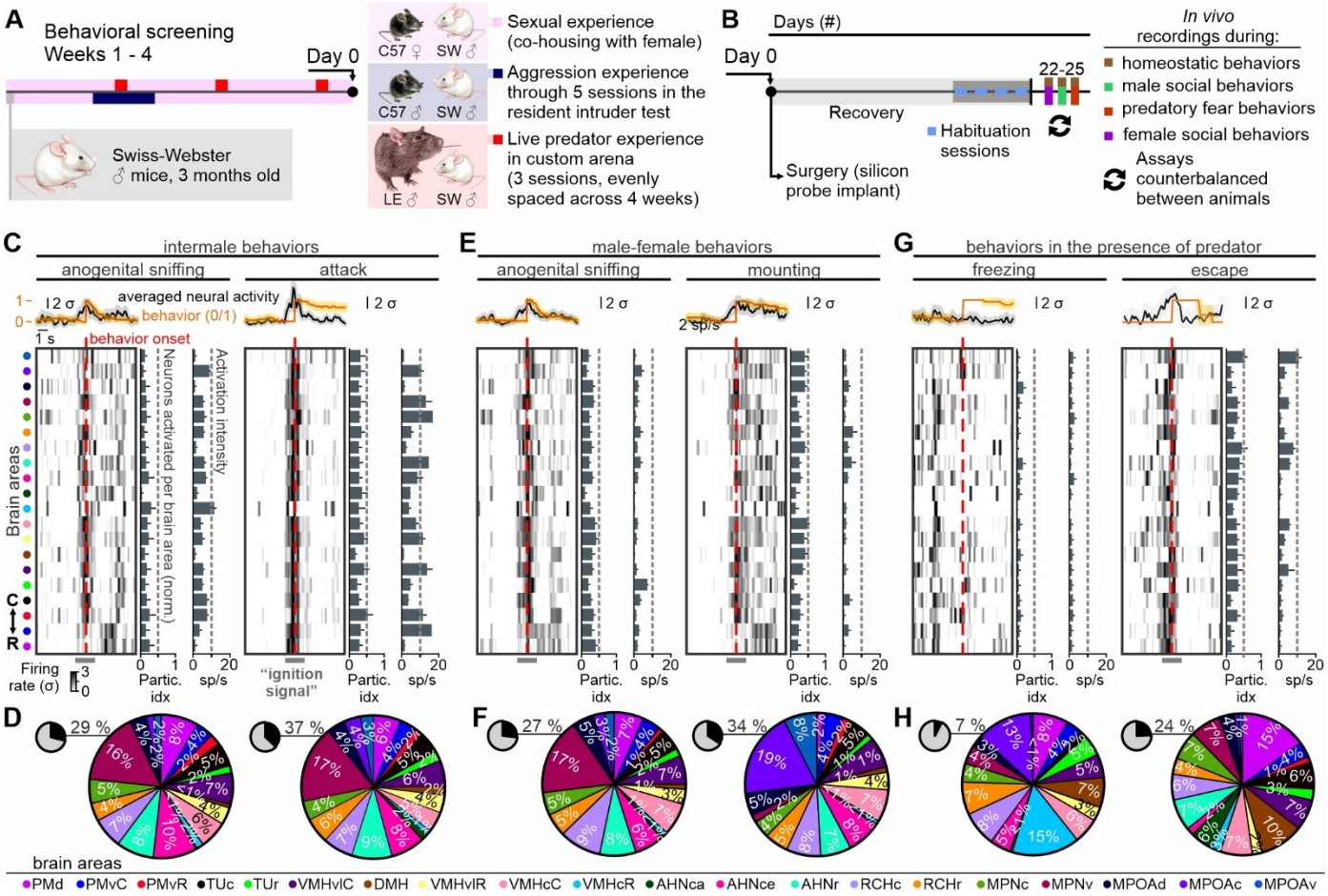


**Fig. 2. Neural ignition signals dominate the peri-onset interval of all instinctual behaviors, apart from freezing to the presence of a predator.** (**A**) Behavioral screening of outbred Swiss Webster mice was used to identify individual mice with prominent behavioral expressions in all of the three behavior paradigms of interest used to assess mating with a female conspecific, aggression against a male conspecific and fear behaviors in the presence of a predator (Long-Evans [LE] rat). Only mice that exhibited appetitive and consummatory behaviors across the three behavior domains (i.e., mating, aggression, and fear), across all behavior screening sessions were selected for chronic silicon probe implant surgery. (**B**) Schematic illustrating the timeline following implantation of the silicon probe. Animals were allowed to fully recover for two weeks in their home cage and were given access to a running wheel. Four habituation sessions were performed (one daily), 4 days prior to the start of the neural recordings

591 and behavior experiments. Habitation sessions included exposure to the exact experimental conditions,
592 in the absence of the stimulus (conspecific, or predator). (**C**) Average behavior signal and mean neural
593 activity at the peri-onset interval of an appetitive and a consummatory intermale social behavior (top).
594 Average neural activity per nucleus (heatmap), participation index (% of neurons activated above 2 SD
595 from baseline activity), and average firing rate of the activated neurons (bottom, n = 6 mice, neural data
596 averaged across three consecutive behavior instances per mouse). (**D**) Small black and gray pie plot:
597 Black – total % of neurons activated, Gray: total % of neurons that did not raise their activity above 2σ.
598 Larger colored pie plot illustrates the spatial coordinates of the neurons that became active (raised their
599 activity >2σ), during male anogenital sniffing (left) and intermale attack (right, n = 6 mice, neural data
600 averaged across three consecutive behavior instances). (**E** and **F**) Same as panels (C) and (D) for an
601 appetitive and a consummatory male-female social behavior. (**G** and **H**) Same as panels (C) and (D) for
602 two predatory fear behaviors.
603 In box-and-whisker plots, center lines indicate medians, box edges represent the interquartile range, and
604 whiskers extend to the minimal and maximal values. See also Fig. S3, S4, and S5. Abbreviations: Partic.
605 Idx.: participation index, sp/s: Firing rate (spikes / sec). Abbreviations of brain areas are described on the
606 legend of Fig. 1.

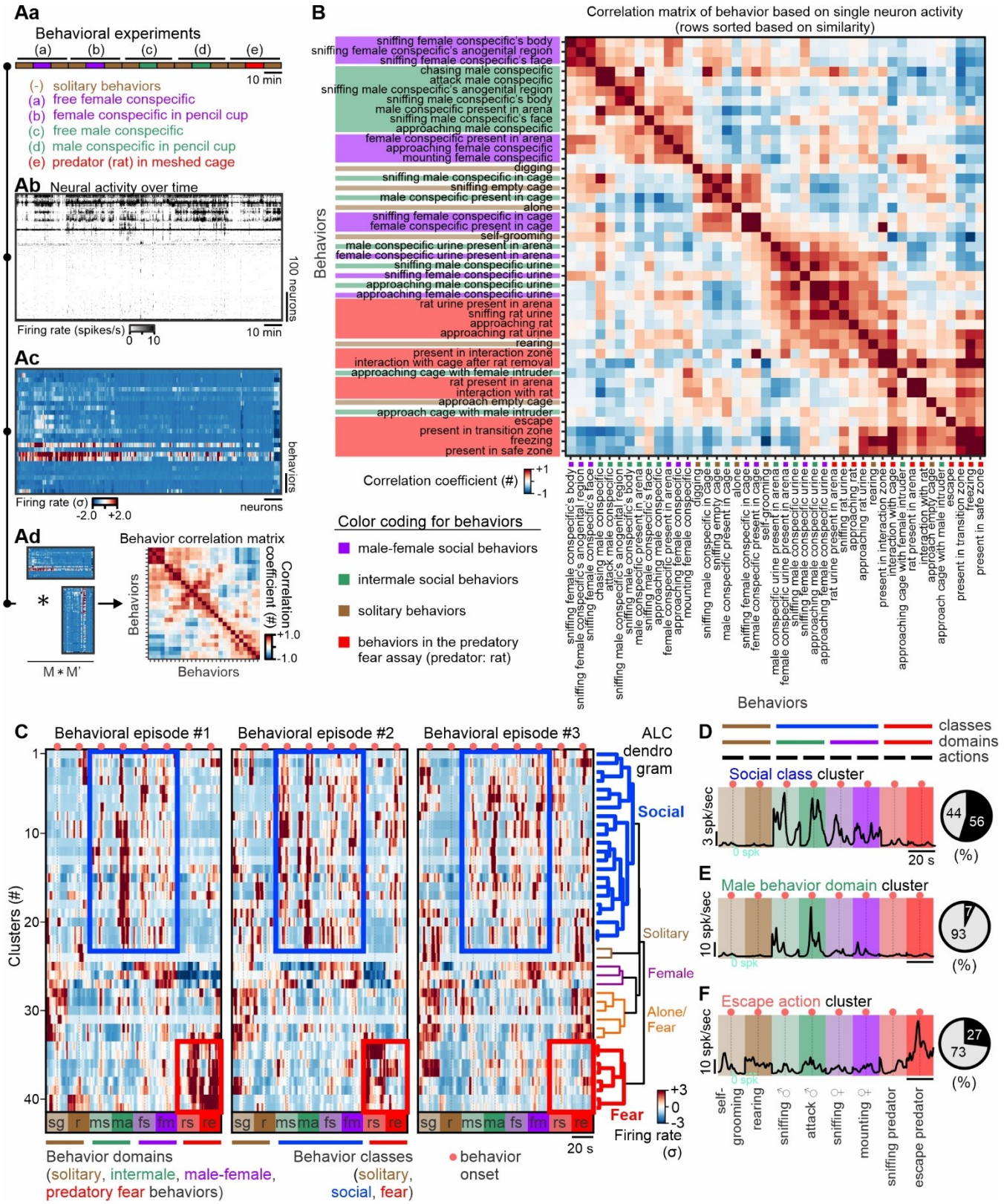
Aa
Behavioral experiments
(a) (b) (c) (d) (e)
10 min
(-) solitary behaviors
(a) free female conspecific
(b) female conspecific in pencil cup
(c) free male conspecific
(d) male conspecific in pencil cup
(e) predator (rat) in meshed cage
Ab Neural activity over time
100 neurons
Firing rate (spikes/s)
0 10
10 min
Ac
behaviors
Firing rate (σ)
-2.0 +2.0
neurons
Ad
Behavior correlation matrix
M * M'
Behaviors
Correlation coefficient (#)
+1.0
-1.0
B
Correlation matrix of behavior based on single neuron activity
(rows sorted based on similarity)
Behaviors
Correlation coefficient (#)
+1
-1
Color coding for behaviors
male-female social behaviors
intermale social behaviors
solitary behaviors
behaviors in the predatory fear assay (predator: rat)
C
Behavioral episode #1
Behavioral episode #2
Behavioral episode #3
ALC dendro gram
Clusters (#)
Social
Solitary
Female
Alone/ Fear
Fear
sg r ms ma fs fm rs re
+3
0
-3
Firing rate (σ)
20 s
Behavior domains (solitary, intermale, male-female, predatory fear behaviors)
Behavior classes (solitary, social, fear)
behavior onset
D
classes
domains
actions
Social class cluster
3 spk/sec
0 spk
20 s
44
56
(%)
E
Male behavior domain cluster
10 spk/sec
0 spk
7
93
(%)
F
Escape action cluster
10 spk/sec
0 spk
27
73
(%)
self-grooming
rearing
sniffing
attack
sniffing
mounting
sniffing predator
escape predator

607

608 **Fig. 3. Encoding of social and fear behavior classes by functionally non-overlapping**
609 **hypothalamic neurons.** (**A**) Analysis design to generate a behaviors correlation matrix. (**Aa**)
610 Experimental conditions. (**Ab**) Single-unit neural activity during the behavioral paradigms shown in Aa.
611 (**Ac**) Z-scored activity of all recorded neurons across solitary-, social-, and fear-behaviors (data from an
612 example mouse). (**Ad**) Multiplication of the matrix shown in ac with its transposed version, results to the
613 behavior covariance matrix, which is then transformed to a behavior correlation matrix. (**B**) Correlation
614 matrix of behavior (average across n = 6 mice). Correlation matrices of behavior of the individual mice
615 can be found in Fig. S7. (**C**) Mean activity of *k*-means clusters explaining 70% of the variance of the
616 single unit data (Extended Data Figure 8). Clusters are sorted using agglomerative linkage clustering to
617 generate a dendrogram whose branches have been assigned semantic labels, based on cluster activity
618 being higher than two standard deviations in specific behavioral classes. (**D**) Left: Mean activity of a *k*-
619 means cluster selected from the forty-one clusters identified and shown in (Fig. 3c), exhibiting mixed
620 selectivity, i.e., activity in diverse behavior domains – in this case, in male-male and male-female
621 behaviors. Right: Portion of clusters showing mixed-selectivity / multi-domain activity. (**E**) Left: Mean
622 activity of a *k*-means cluster selected from the forty-one clusters identified (Fig. 3C), showing mixed
623 selectivity within a behavioral domain – in this case, in intermale behaviors. Right: Portion of clusters
624 showing mixed selectivity within a behavioral domain (alone / intermale / male-female / and fear
625 behaviors). (**F**) Left: Mean activity of a *k*-means cluster selected from the forty-one clusters identified (Fig.
626 3c), showing behavior-specific tuning – in this case, in escape response to a predator. Right: Portion of
627 clusters showing behavior action-specific tuning.
628 Abbreviations: sg: self-grooming, r: rearing, ms: male intruder anogenital sniffing, ma: intermale attack,
629 fs: female intruder anogenital sniffing, fm: mounting female intruder, rs: sniffing predator, re: escape
630 response to a predator. See also Fig. S7, S8, and S9.

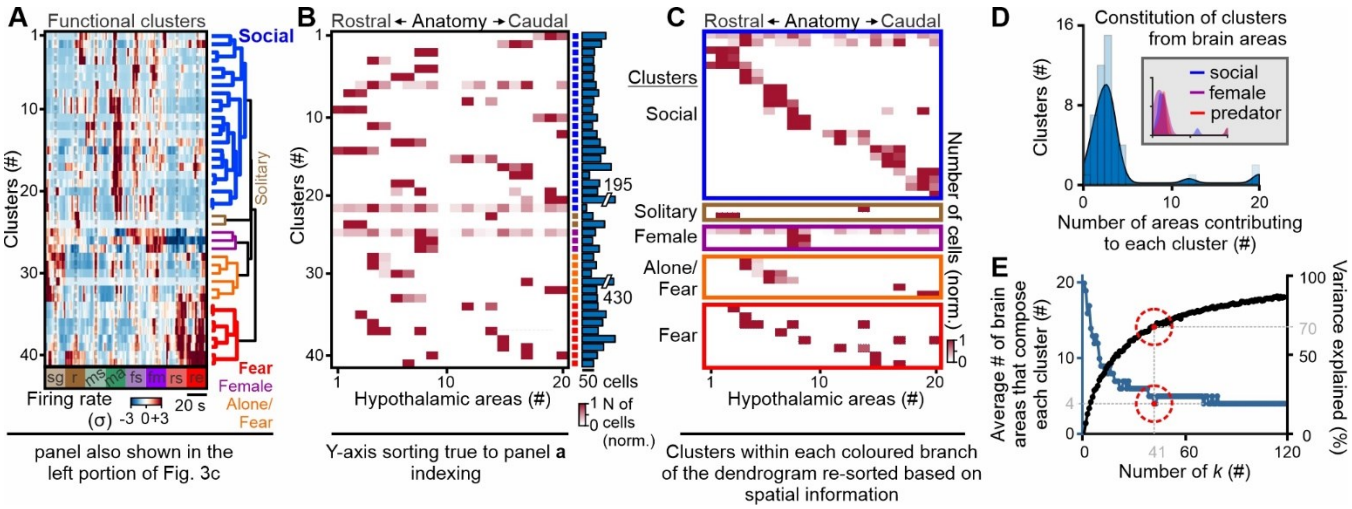


**Fig. 4. Encoding of behavior classes is spatially distributed, but single clusters are spatially localized.** (**A**) Functional clusters of single neuron activity (panel from Fig. 3c – left). (**B**) Spatial composition of each of the 41 functional clusters shown in panel (A). (**C**) Re-sorting the spatial composition of each cluster, to present clusters composed of most rostral regions, to clusters composed of most caudal regions. (**D**) Histogram of hypothalamic area contribution per cluster. Inset: Histogram of hypothalamic area contribution to clusters that are active in specific behaviors. (**E**) Spatial composition of clusters based on the choice of *k* (number of clusters selected for *k*-means clustering), reveals that the average composition of a cluster by four regions is a stable solution.

Abbreviations: sg: self-grooming, r: rearing, ms: male intruder anogenital sniffing, ma: intermale attack, fs: female intruder anogenital sniffing, fm: mounting female intruder, rs: sniffing predator, re: escape response to a predator. See also Fig. S9, B-D.

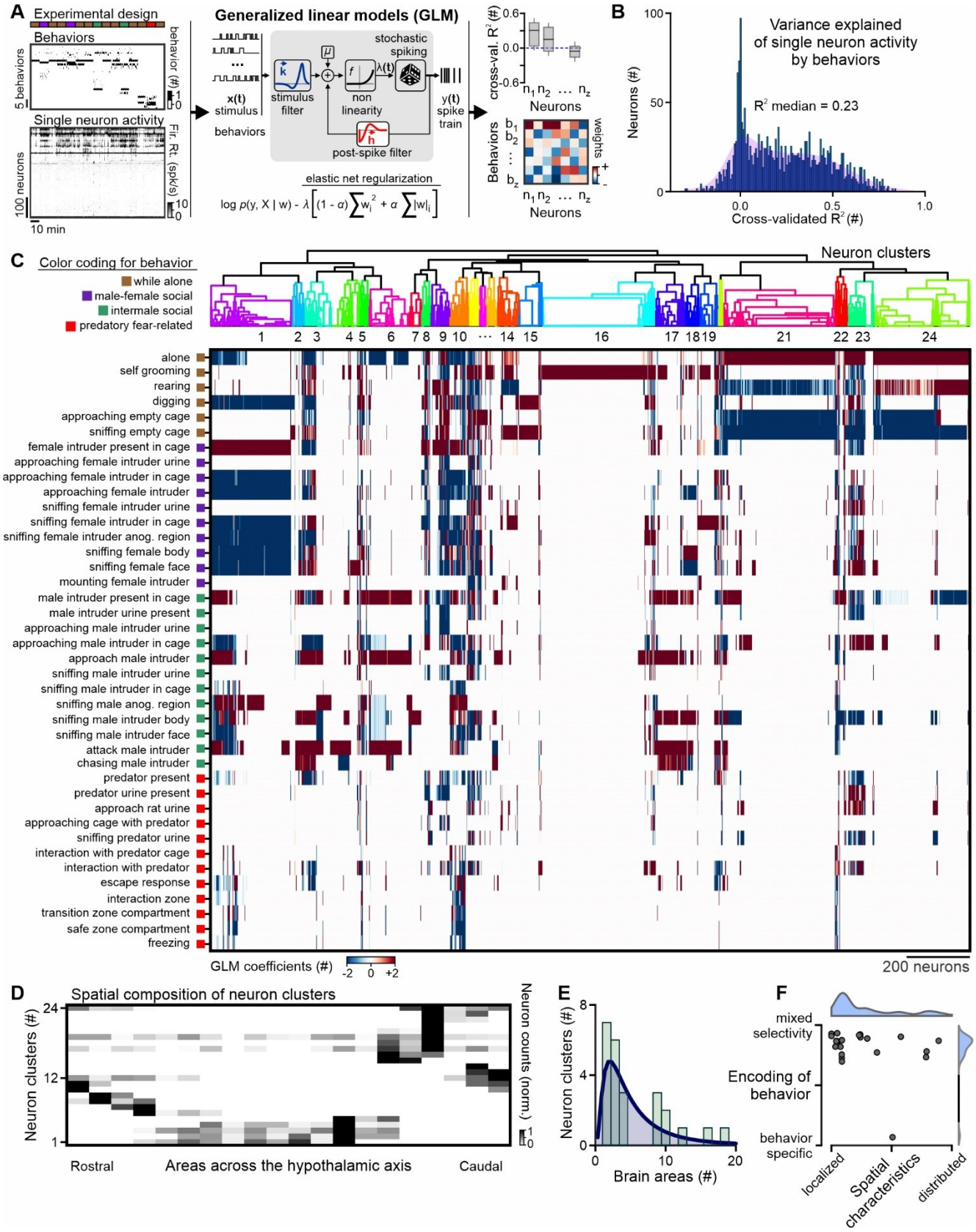
A
Experimental design
Behaviors
5 behaviors
behavior (#)
Single neuron activity
100 neurons
Fir. Rt. (spk/s)
10 min
Generalized linear models (GLM)
x(t)
stimulus
behaviors
stimulus filter
non linearity
stochastic spiking
post-spike filter
y(t)
spike train
elastic net regularization
cross-val. R² (#)
Neurons
Behaviors
weights
B
Variance explained of single neuron activity by behaviors
R² median = 0.23
Neurons (#)
Cross-validated R² (#)
C
Color coding for behavior
while alone
male-female social
intermale social
predatory fear-related
Neuron clusters
alone
self grooming
rearing
digging
approaching empty cage
sniffing empty cage
female intruder present in cage
approaching female intruder urine
approaching female intruder in cage
approaching female intruder
sniffing female intruder urine
sniffing female intruder in cage
sniffing female intruder anog. region
sniffing female body
sniffing female face
mounting female intruder
male intruder present in cage
male intruder urine present
approaching male intruder urine
approaching male intruder in cage
approach male intruder
sniffing male intruder urine
sniffing male intruder in cage
sniffing male anog. region
sniffing male intruder body
sniffing male intruder face
attack male intruder
chasing male intruder
predator present
predator urine present
approach rat urine
approaching cage with predator
sniffing predator urine
interaction with predator cage
interaction with predator
escape response
interaction zone
transition zone compartment
safe zone compartment
freezing
GLM coefficients (#)
200 neurons
D
Spatial composition of neuron clusters
Neuron clusters (#)
Neuron counts (norm.)
Rostral
Areas across the hypothalamic axis
Caudal
E
Neuron clusters (#)
Brain areas (#)
F
mixed selectivity
Encoding of behavior
behavior specific
localized
Spatial characteristics
distributed

643

644 **Fig. 5. Solitary, social and fear behaviors explain a quarter of hypothalamic neuron activity**
645 **variance and suggest a spatial organization of functional neuron clusters.** (**A**) Analysis design using
646 generalized linear models (GLMs) to study the encoding of behavior by non-genetically defined
647 mesoscale hypothalamic populations. (**B**) Variance explained (cross-validated, shuffled data $R^2$
648 subtracted, $R^2$) of single-neuron activity (n=6 mice, 2347 neurons) based on forty-two instinctual
649 behaviors. (**C**) Agglomerative linkage clustering of behavior GLM-generated coefficients into twenty-four
650 neural dendrogram branches/clusters. (**D**) Average neuron counts per brain area across the
651 hypothalamic rostro-caudal axis across all neural branches, reveals a spatial bias of neural branch
652 composition. (**E**) Histogram of hypothalamic area contribution per cluster. (**F**) Spatial vs. functional
653 characteristics of neuron clusters.
654 In box-and-whisker plots, center lines indicate medians, box edges represent the interquartile range, and
655 whiskers extend to the minimal and maximal values. See also Fig. S11, S12, and S13.

# Extended Data Figures

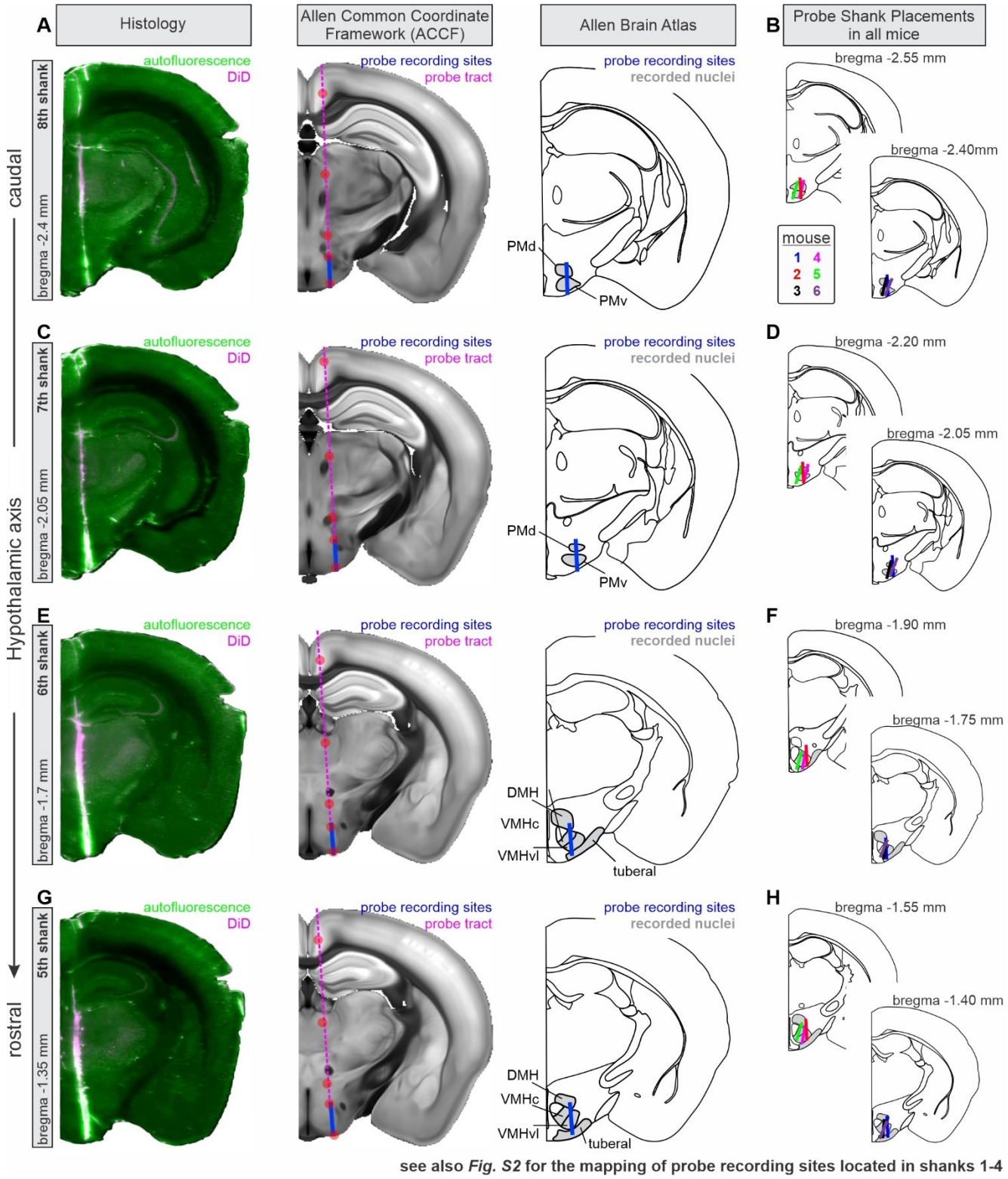


**Fig. S1. Mapping of recording sites across the medial-caudal hypothalamus.** (**A**) Left: Computationally sectioned coronal view of the mouse brain that includes the eighth shank of the chronic silicon probe implant. Center and Right: Mapping the shank and the electrode-containing area of the

shank to the Allen Common Coordinate Framework (example section/mouse). (**B**) Mapping the overlap of all recording electrodes of the eighth shank across all probes/mice to the caudal hypothalamic areas (PMd: dorsal premammillary nucleus, and PMv: ventral premammillary nucleus, n=6 mice). (**C**) Left: Computationally sectioned coronal view of the mouse brain that includes the seventh shank of the chronic silicon probe implant. Center and Right: Mapping the shank and the electrode-containing area of the shank to the Allen Common Coordinate Framework (example section/mouse). (**D**) Mapping the overlap of all recording electrodes of the seventh shank across all probes/mice to the caudal hypothalamic areas (PMd: dorsal premammillary nucleus, and PMv: ventral premammillary nucleus, n=6 mice). (**E**) Left: Computationally sectioned coronal view of the mouse brain that includes the sixth shank of the chronic silicon probe implant. Center and Right: Mapping the shank and the electrode-containing area of the shank to the Allen Common Coordinate Framework (example section/mouse). (**F**) Mapping the overlap of all recording electrodes of the sixth shank across all probes/mice to the medial-caudal hypothalamic areas (DMH: dorsomedial hypothalamic nucleus, VMHc: ventromedial hypothalamic nucleus central segment, VMHvl: ventromedial hypothalamic nucleus ventrolateral segment, and tuberal nucleus, n=6 mice). (**G**) Left: Computationally sectioned coronal view of the mouse brain that includes the fifth shank of the chronic silicon probe implant. Center and Right: Mapping the shank and the electrode-containing area of the shank to the Allen Common Coordinate Framework (example section/mouse). (**H**) Mapping the overlap of all recording electrodes of the fifth shank across all probes/mice to the medial-caudal hypothalamic areas (DMH: dorsomedial hypothalamic nucleus, VMHc: ventromedial hypothalamic nucleus central segment, VMHvl: ventromedial hypothalamic nucleus ventrolateral segment, and tuberal nucleus, n=6 mice).

Figure relevant to Fig. 1.

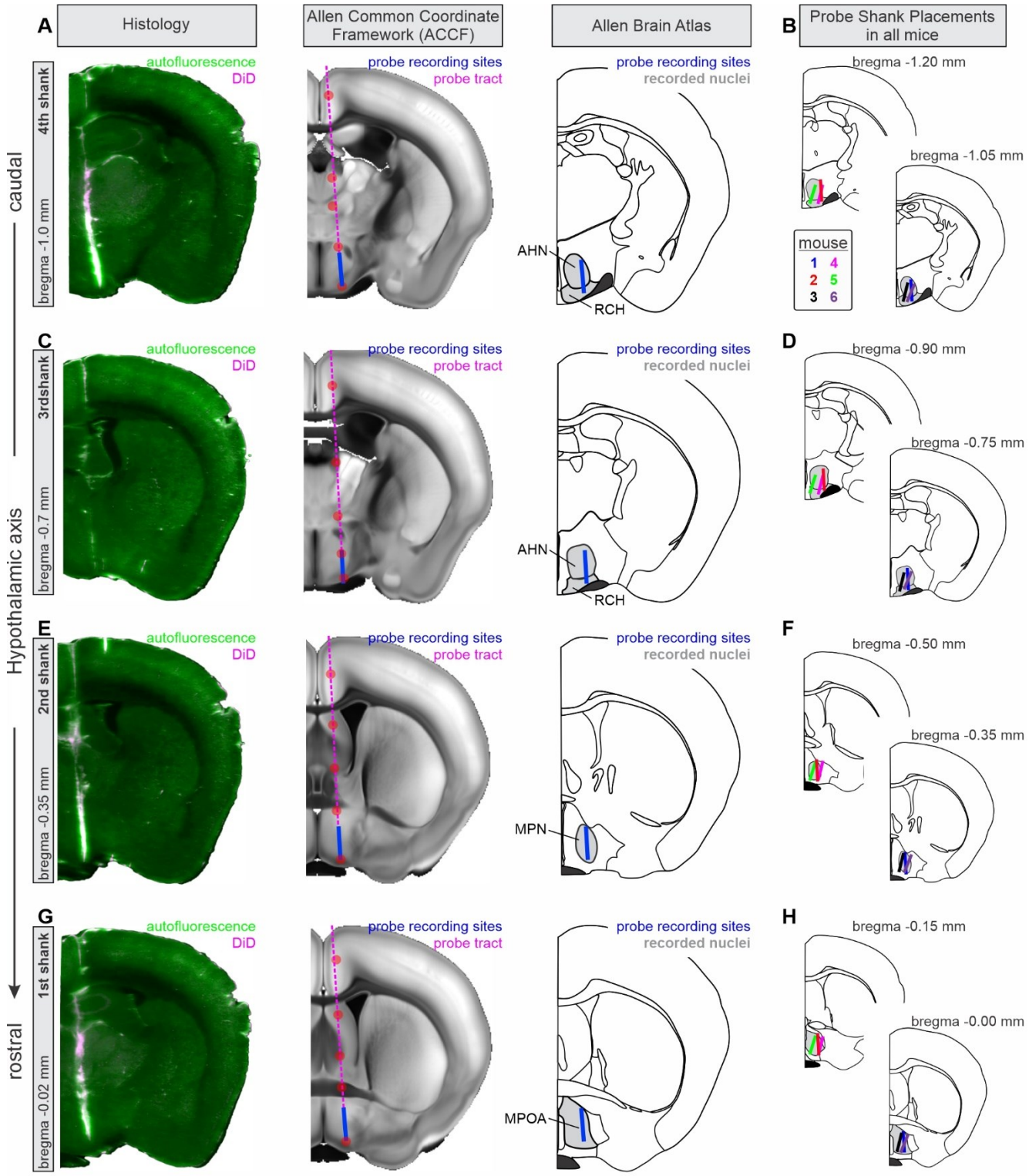


**Fig. S2. Mapping of recording sites across the medial-rostral hypothalamus.** (**A**) Left: Computationally sectioned coronal view of the mouse brain that includes the fourth shank of the chronic

689 silicon probe implant. Center and Right: Mapping the shank and the electrode-containing area of the
690 shank to the Allen Common Coordinate Framework (example section/mouse). (**B**) Mapping the overlap
691 of all recording electrodes of the fourth shank across all probes/mice to the caudal hypothalamic areas
692 (RCH: retrochiasmatic area, and AHN: anterior hypothalamic nucleus, n=6 mice). (**C**) Left:
693 Computationally sectioned coronal view of the mouse brain that includes the third shank of the chronic
694 silicon probe implant. Center and Right: Mapping the shank and the electrode-containing area of the
695 shank to the Allen Common Coordinate Framework (example section/mouse). (**D**) Mapping the overlap
696 of all recording electrodes of the third shank across all probes/mice to the medial-rostral hypothalamic
697 areas (RCH: retrochiasmatic area and AHN: anterior hypothalamic nucleus, n=6 mice). (**E**) Left:
698 Computationally sectioned coronal view of the mouse brain that includes the second shank of the chronic
699 silicon probe implant. Center and Right: Mapping the shank and the electrode-containing area of the
700 shank to the Allen Common Coordinate Framework (example section/mouse). (**F**) Mapping the overlap
701 of all recording electrodes of the second shank across all probes/mice to the medial-rostral hypothalamic
702 areas (MPN: medial preoptic nucleus, n=6 mice). (**G**) Left: Computationally sectioned coronal view of the
703 mouse brain that includes the first shank of the chronic silicon probe implant. Center and Right: Mapping
704 the shank and the electrode-containing area of the shank to the Allen Common Coordinate Framework
705 (example section/mouse). (**H**) Mapping the overlap of all recording electrodes of the first shank across
706 all probes/mice to the rostral hypothalamic areas (MPOA: medial preoptic area, n=6 mice).
707 Figure relevant to Fig. 1.

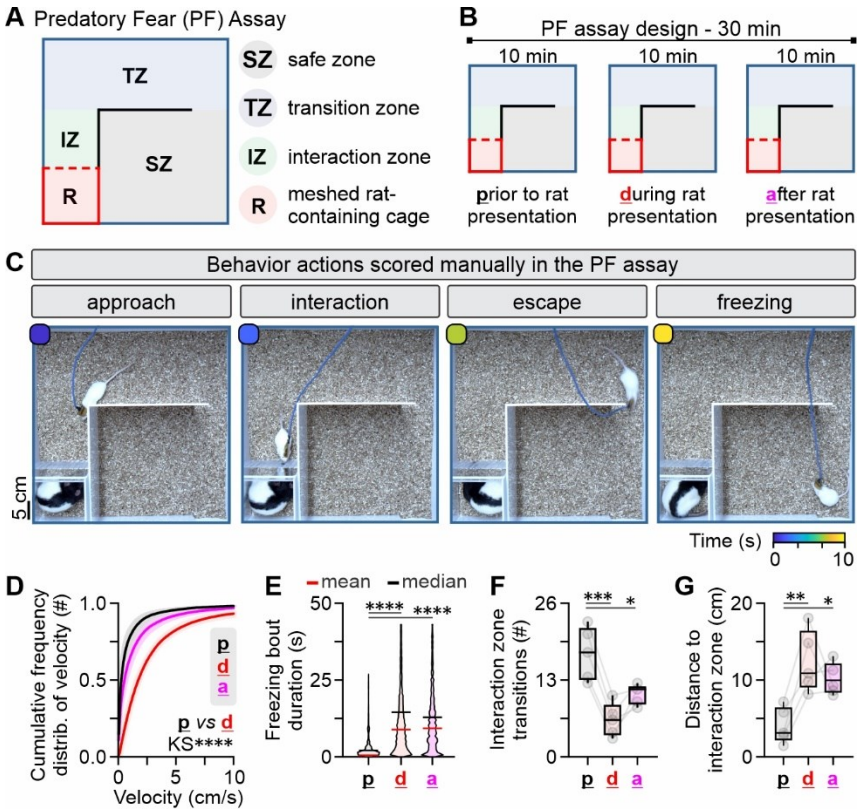


708

709 **Fig. S3. Quantification of behavior in the predatory fear assay.** (**A**) Experimental design of a custom
710 predatory fear assay, with four compartments. R: compartment containing the predator (rat), with a single,
711 clear, and perforated side facing the compartment IZ, i.e., interaction compartment. TZ: is the transition
712 compartment that links compartments R and SZ, the latter furthest away from the predator. (**B**) Timeline
713 of the behavioral experiments with the fear condition flanked by two periods where the implanted mouse
714 is alone in the arena. (**C**) Snapshots illustrating four manually annotated behaviors, specifically;
715 approaching the predator, interacting with the predator, escape response to a predator (a high-velocity
716 activity bout towards the safe zone compartment), and freezing behavior (observed in the freezing
717 compartment). (**D**) Frequency distribution of velocity during the three conditions shown in panel (B). (**E**)
718 Freezing bout duration in the three conditions presented in in panel (B). (**F**) Number of crosses of the
719 interaction zone across the three conditions presented in panel (B). (**G**) Distance to interaction zone
720 among the three conditions presented in panel (B).

721 *$P < 0.05$, **$P < 0.01$, ***$P < 0.001$, ****$P < 0.0001$. Statistical comparisons of the data illustrated in panel
722 (D) were performed by the Kolmogorov-Smirnov test, while comparisons of the data shown in panels (E-
723 G) were performed through One-Way ANOVA and Dunnett's post-hoc test was used to correct for
724 multiple comparisons. In box-and-whisker plots, center lines indicate medians, box edges represent the
725 interquartile range, and whiskers extend to the minimal and maximal values. Figure relevant to Fig. 2.

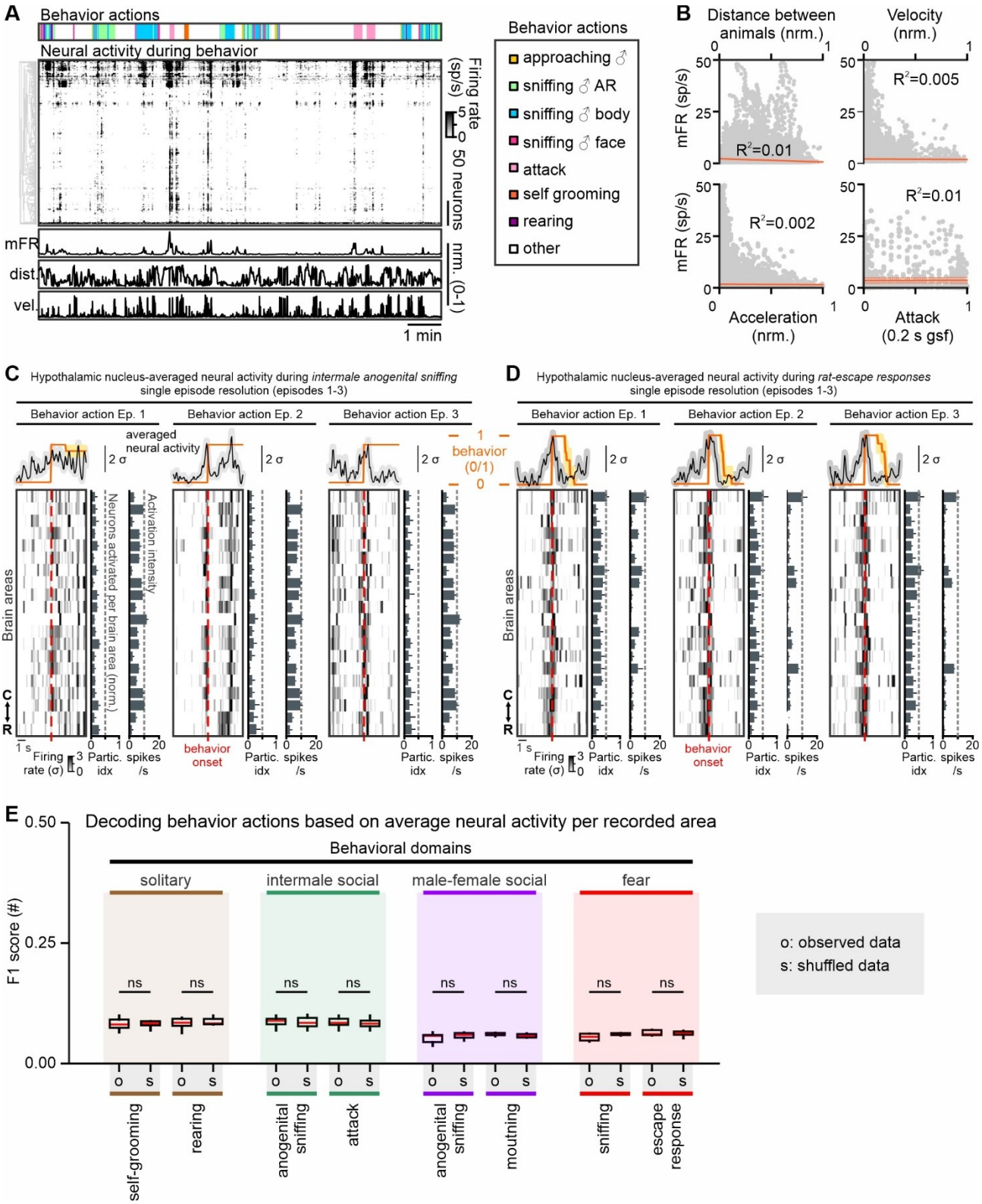
A
Behavior actions
Neural activity during behavior
Firing rate (sp/s)
50 neurons
mFR
dist
vel
nrm. (0-1)
1 min
Behavior actions
approaching ♂
sniffing ♂ AR
sniffing ♂ body
sniffing ♂ face
attack
self grooming
rearing
other
B
Distance between animals (nrm.)
Velocity (nrm.)
mFR (sp/s)
R²=0.01
R²=0.005
R²=0.002
R²=0.01
Acceleration (nrm.)
Attack (0.2 s gsf)
C
Hypothalamic nucleus-averaged neural activity during intermale anogenital sniffing
single episode resolution (episodes 1-3)
Behavior action Ep. 1
Behavior action Ep. 2
Behavior action Ep. 3
averaged neural activity
behavior (0/1)
Brain areas
Neurons activated per brain area (norm.)
Activation intensity
behavior onset
Firing rate (σ)
Partic. idx
spikes /s
D
Hypothalamic nucleus-averaged neural activity during rat-escape responses
single episode resolution (episodes 1-3)
E
Decoding behavior actions based on average neural activity per recorded area
Behavioral domains
solitary
intermale social
male-female social
fear
F1 score (#)
ns
o: observed data
s: shuffled data
self-grooming
rearing
anogenital sniffing
attack
anogenital sniffing
moutning
sniffing
escape response

726

**Fig. S4. Motion variables including distance between animals and animal's velocity, do not correlate with the mean firing rate of hypothalamic neurons, ignition signals occur across behavioral action episodes, and behavior actions are not decodable based on nucleus-averaged neural activity.** (**A**) Example time series data of behavior, single neuron activity, mean firing rate, distance between animals, and velocity of recorded mouse. (**B**) Average behavior signal and mean neural activity at the peri-onset interval of predator-directed anogenital sniffing, in three behavioral episodes (top). Average neural activity per nucleus (heatmap), participation index (% of neurons activated above 2 SD from baseline activity), and average firing rate of the activated neurons (bottom, n = 6 mice, in three behavior episodes per mouse). (**C**) Average behavior signal and mean neural activity at the peri-onset interval of escape responses in the presence of a predator, in three behavioral episodes (top). Average neural activity per nucleus (heatmap), participation index (% of neurons activated above 2 SD from baseline activity), and average firing rate of the activated neurons (bottom, n = 6 mice, in three behavior episodes per mouse). (**D**) Correlation analysis of motion variables and average firing rate (n=6 mice, data pooled across mice). (**E**) SVM decoder F1 score on behavior actions of interest based on nucleus-averaged neural activity (n = 6 mice).

Abbreviations: mFR: mean firing rate all recorded neurons, dist.: distance between animals, vel.: velocity, sp/s: spikes per second, nrm.: data normalized between 0 and 1 values, 0.2 s gsf: 200 millisecond gaussian smoothing filter applied on the spike and behavior data prior to performing linear regression. Figure relevant to Fig. 2.

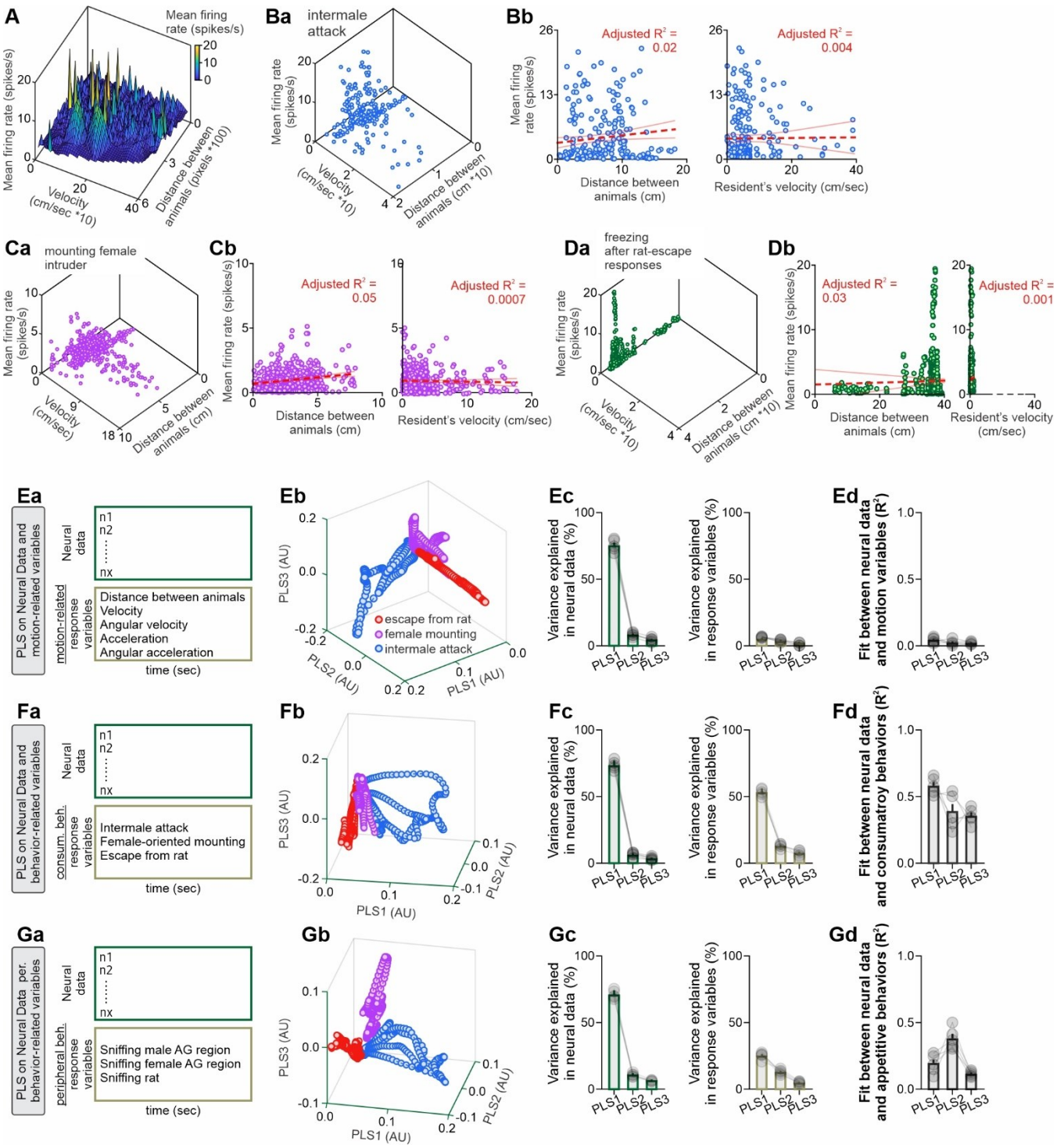


**Fig. S5. Consummatory instinctual behaviors have stronger representation in hypothalamic neural data, as opposed to appetitive behaviors and motion-related variables.** (**A**) Landscape of neural activity vs. velocity of implanted mouse and distance between animals (pooled data across six

750 mice). (**Ba**) Plotting of mean firing rate vs. velocity of implanted mouse and distance between animals
751 during the duration of intermale attack instances. (**Bb**) Linear regression between mean firing rate and
752 velocity, and mean firing rate and distance between animals during the duration of intermale attack
753 instances (pooled data across six mice). (**Ca**) Plotting of mean firing rate vs. velocity of implanted mouse
754 and distance between animals during the duration of mounting a female conspecific. (**Cb**) Linear
755 regression between mean firing rate and velocity, and mean firing rate and distance between animals
756 during the duration of mounting a female conspecific (pooled data across six mice). (**Da**) Plotting of mean
757 firing rate vs. velocity of implanted mouse and distance between animals during instances of freezing in
758 the predatory-fear assay. (**Db**) Linear regression between mean firing rate and velocity, and mean firing
759 rate and distance between animals during instances of freezing in the predatory-fear assay (pooled data
760 across six mice). (**Ea**) Analysis design and input to partial least-squares regression, to assess the
761 correlation between partial least-square components between neural data and motion-related variables.
762 (**Eb**) Neural trajectories of PLS components in the PLS-space (example mouse). (**Ec**) Left: Variance
763 explained by PLS components of the single-unit neural data. Right: Variance explained by PLS
764 components of the motion-related variables (n=6 mice). (**Ed**) Fit between neural and motion-variable PLS
765 components, indicative of a poor link between the two types of data (n=6 mice). (**Fa**) Analysis design and
766 input to partial least-squares regression, to assess the correlation between partial least-square
767 components between neural data and consummatory social and fear behaviors. (**Fb**) Neural trajectories
768 of PLS components in the PLS-space (example mouse). (**Fc**) Left: Variance explained by PLS
769 components of the single-unit neural data. Right: Variance explained by PLS components of the
770 consummatory social and fear behaviors (n=6 mice). (**Fd**) Fit between neural and consummatory
771 instinctual behavior-based PLS components, indicative of a link between the two types of data (n=6 mice).
772 (**Ga**) Analysis design and input to partial least-squares regression, to assess the correlation between
773 partial least-square components between neural data and appetitive social and fear behaviors. (**Gb**)
774 Neural trajectories of PLS components in the PLS-space (example mouse). (**Gc**) Left: Variance explained
775 by PLS components of the single-unit neural data. Right: Variance explained by PLS components of the

appetitive social and fear behaviors (n=6 mice). (**Gd**) Fit between neural and appetitive social and fear behavior-based PLS components, indicative of a link between the two types of data (n=6 mice). Figure relevant to Fig. 2.

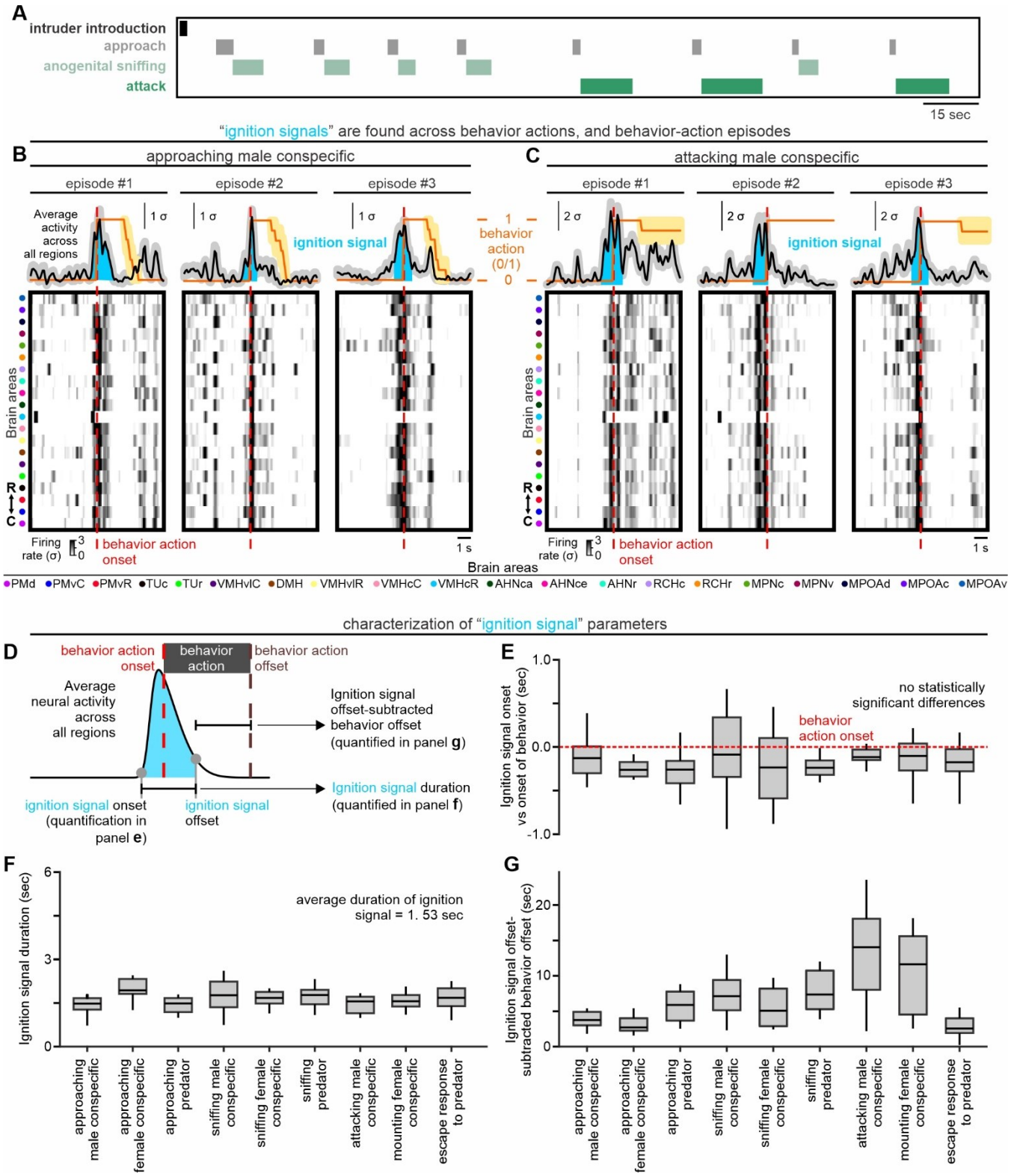


**Fig. S6. "Ignition signals" occur across social and fear behaviors, across behavioral episodes,**

**typically 200 msec prior to behavior onset, and have an average duration of 1.5 seconds.** (**A**) Example behavior raster plot indicating the repetitive nature of specific intermale behaviors following the introduction of a male intruder in the resident-intruder assay. (**B**) Ignition signals (highlighted in light blue) occur across behavior action episodes of approaching a male conspecific (n = 6 mice). (**C**), Ignition signals (highlighted in light blue) occur across behavior action episodes of attacking a male conspecific (n = 6 mice). (**D**) Characteristics of ignition signals include onset, offset and duration relevant to behavior. E, Quantification of the onset of ignition signals relevant to the onset of behavior (n = 6 mice, neural data averaged across three consecutive behavior instances per mouse). (**F**) Quantification of the ignition signal duration (n = 6 mice, neural data averaged across three consecutive behavior instances per mouse). (**G**) Quantification of the ignition signal offset subtracted behavior offset (n = 6 mice, neural data averaged across three consecutive behavior instances per mouse).

In box-and-whisker plots, center lines indicate medians, box edges represent the interquartile range, and whiskers extend to the minimal and maximal values. Abbreviations of brain areas are described in the legend of Figure 1. Statistical comparisons of the data shown in panel (E-G) were performed through One-Way ANOVA and Tukey's post-hoc test was used to correct for multiple comparisons. In box-and-whisker plots, center lines indicate medians, box edges represent the interquartile range, and whiskers extend to the minimal and maximal values. Figure relevant to Fig. 2.

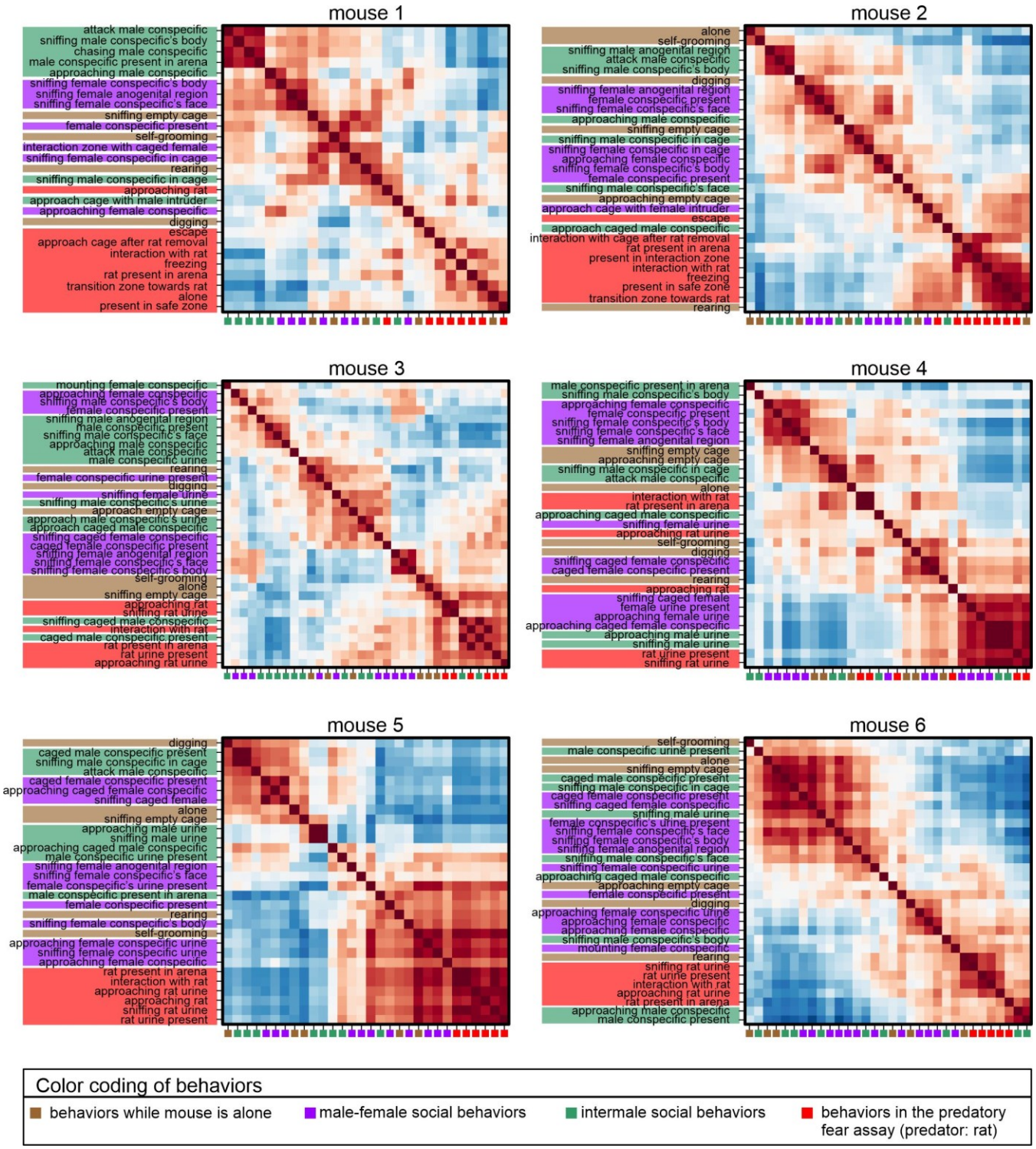


**Fig. S7. Correlation matrix of behavior for each of the recorded six mice, with behavior actions sorted based on similarity.** Note the relative segregation of fear behavior actions (marked in red)

800 towards the end of the row labels in each matrix, while other behaviors are intermingled. Figure relevant

801 to Fig. 3, A and B.

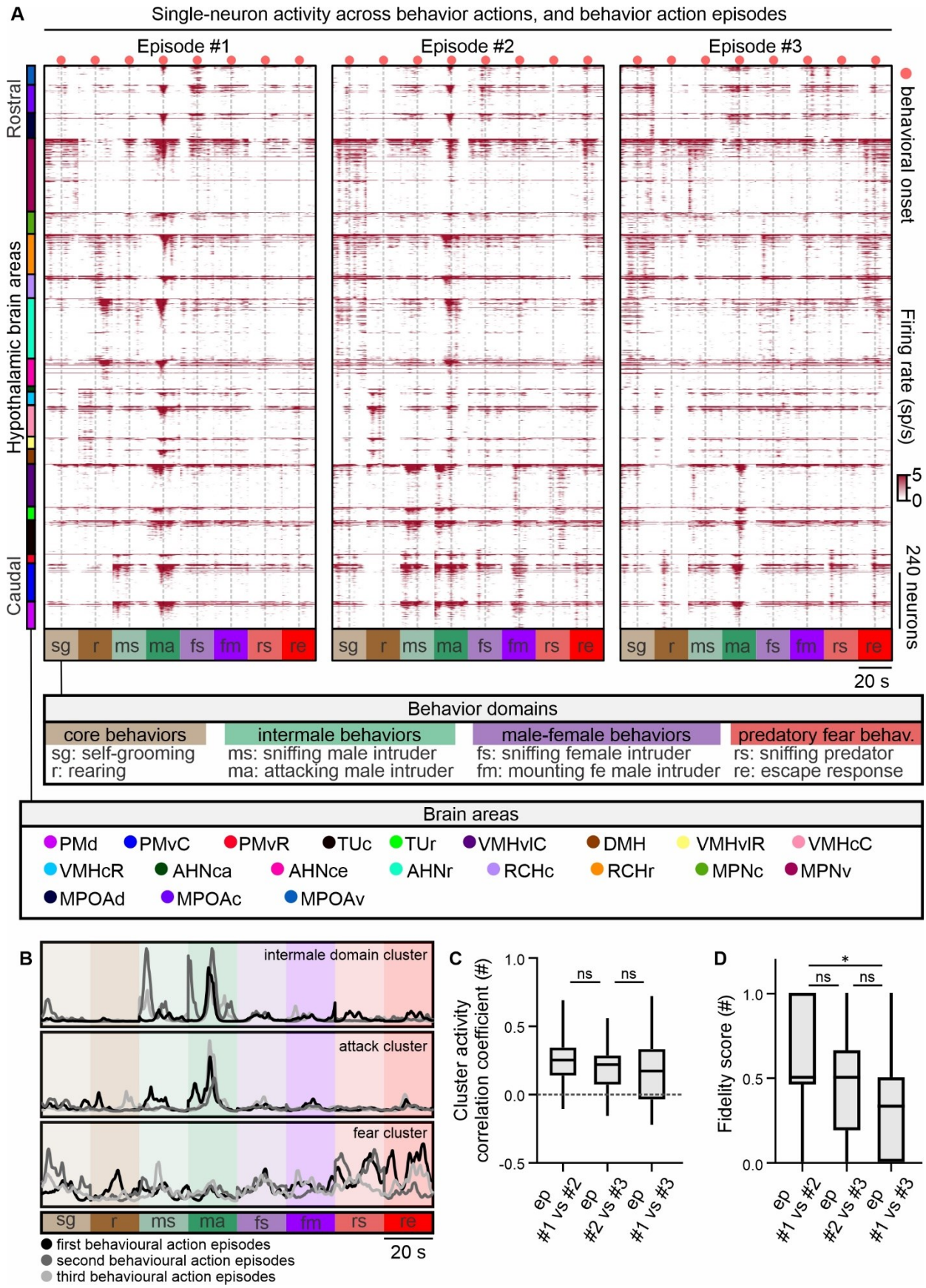
A
Single-neuron activity across behavior actions, and behavior action episodes
Episode #1
Episode #2
Episode #3
Rostral
Hypothalamic brain areas
Caudal
behavioral onset
Firing rate (sp/s)
5
0
240 neurons
sg r ms ma fs fm rs re
20 s
Behavior domains
core behaviors
sg: self-grooming
r: rearing
intermale behaviors
ms: sniffing male intruder
ma: attacking male intruder
male-female behaviors
fs: sniffing female intruder
fm: mounting fe male intruder
predatory fear behav.
rs: sniffing predator
re: escape response
Brain areas
PMd PMvC PMvR TUc TUr VMHvlC DMH VMHvlR VMHcC
VMHcR AHNca AHNce AHNr RCHc RCHr MPNc MPNv
MPOAd MPOAc MPOAv
B
intermale domain cluster
attack cluster
fear cluster
first behavioural action episodes
second behavioural action episodes
third behavioural action episodes
C
Cluster activity correlation coefficient (#)
ns
ep #1 vs #2
ep #2 vs #3
ep #1 vs #3
D
Fidelity score (#)
*

802

**Fig. S8. Single unit activity across four behavior domains, eight behaviors of interest, and three behavior episodes.** (**A**) Single unit activity in eight behaviors of interest during three consecutive behavioral episodes/instances (n=6 mice, 2347 neurons). (**B**) Selected clusters from panel c Fig. 3, indicating the activity of each cluster across the first, second and third behavioral action episodes. (**C**) Correlation coefficient of average cluster activity across behavioral episodes (relevant to Fig. 3C). (**D**) Fidelity score of cluster identity across behavior episodes; a measure that quantifies the degree to which a cluster is active to the exact same behavior(s). A cluster considered active during the expression of any single behavior, scales its activity above the threshold of two standard deviations (as compared to its baseline activity).

ns: statistically not significant, $*P < 0.05$. Statistical comparisons of the data shown in panels (B, C) were performed through One-Way ANOVA and Dunnett's post-hoc test was used to correct for multiple comparisons. In box-and-whisker plots, center lines indicate medians, box edges represent the interquartile range, and whiskers extend to the minimal and maximal values. Figure relevant to Fig. 3.

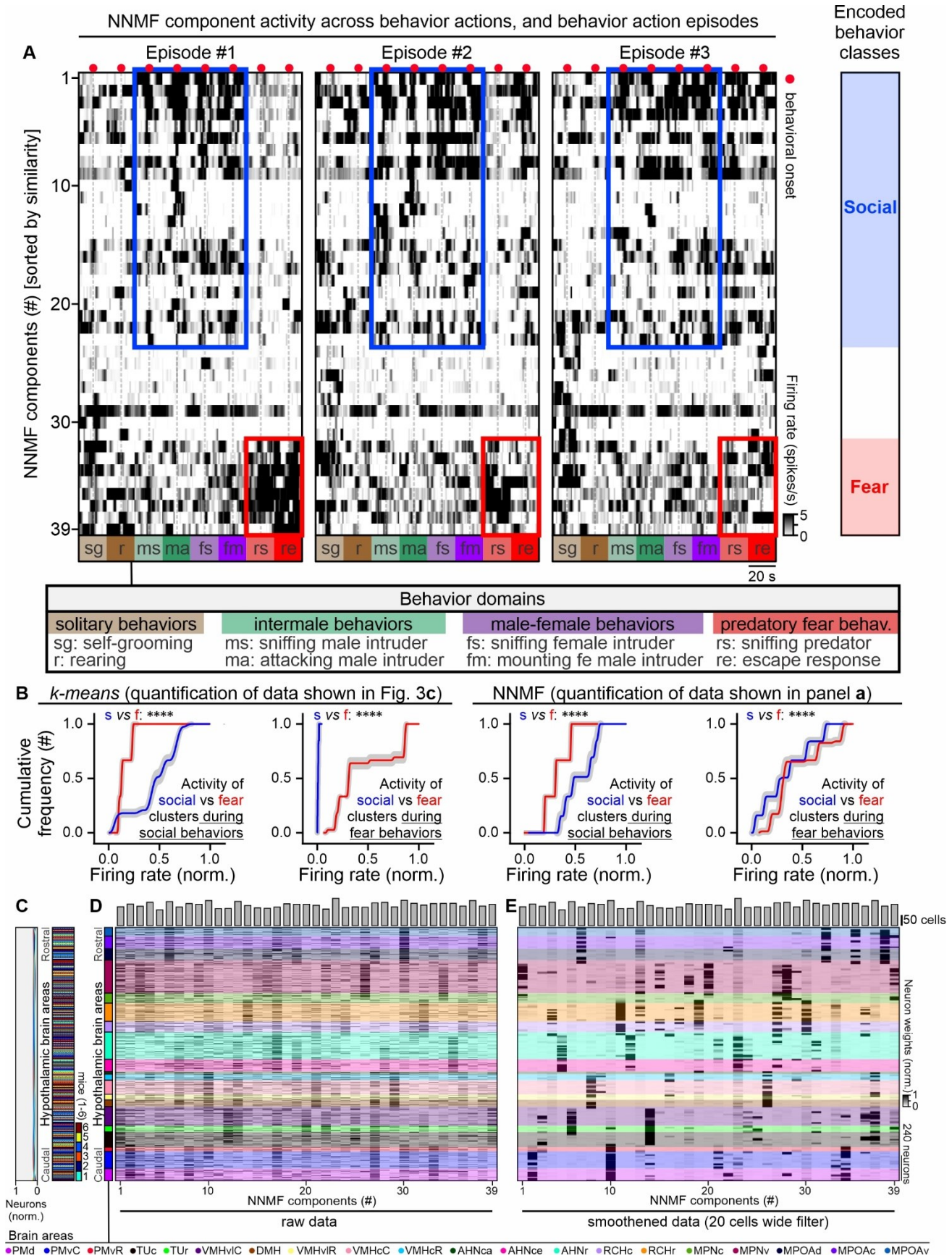
NNMF component activity across behavior actions, and behavior action episodes
Encoded behavior classes
A
Episode #1
Episode #2
Episode #3
NNMF components (#) [sorted by similarity]
behavioral onset
Firing rate (spikes/s)
Social
Fear
sg r ms ma fs fm rs re
20 s
Behavior domains
solitary behaviors
sg: self-grooming
r: rearing
intermale behaviors
ms: sniffing male intruder
ma: attacking male intruder
male-female behaviors
fs: sniffing female intruder
fm: mounting fe male intruder
predatory fear behav.
rs: sniffing predator
re: escape response
B
k-means (quantification of data shown in Fig. 3c)
NNMF (quantification of data shown in panel a)
Cumulative frequency (#)
s vs f: ****
Activity of social vs fear clusters during social behaviors
Activity of social vs fear clusters during fear behaviors
Firing rate (norm.)
C
D
E
Rostral
Hypothalamic brain areas
Caudal
mice (1-6)
Neurons (norm.)
NNMF components (#)
raw data
smoothened data (20 cells wide filter)
50 cells
Neuron weights (norm.)
240 neurons
Brain areas
PMd PMvC PMvR TUc TUr VMHvlC DMH VMHvlR VMHcC VMHcR AHNca AHNce AHNr RCHc RCHr MPNc MPNv MPOAd MPOAc MPOAv

817 **Fig. S9. Non-negative matrix factorization (NMF) identifies ensembles with behavior class**
818 **specificity and spatial bias.** (**A**) NMF matrix factorization of the single neuron activity data shown in
819 Extended Data Fig. 8, generates 39 NMF components (collectively explaining 79% of the variance of the
820 single unit data, a number selected using the elbow method). Activity of components occurs somewhat
821 similarly to the *k*-means clusters identified and shown in Fig. 3, during the social and fear behavior
822 classes. (**B**) Cumulative frequency of recorded firing rates in "social" or "fear" clusters identified in the *k*-
823 means (Fig. 3) and NMF (present figure) analysis respectively. Note that cluster activity is significantly
824 different between conditions, but magnitude of effect is smaller in the NMF analysis. (**C**) Histogram (left)
825 and raster plot (right) showing neuron origin from the six recorded mice. (**D**) Neuron weights of the NMF
826 components (raw data, n=6 mice). (**E**) Neuron weights of the NMF components (smoothened data
827 [Gaussian smoothing filter with twenty cells size], n=6 mice).
828 ****$P < 0.0001$. Statistical comparisons were performed through the Kolmogorov-Smirnov test.
829 Abbreviations of brain areas presented in the legend of Figure 1. Figure relevant to Fig. 3 and 4.

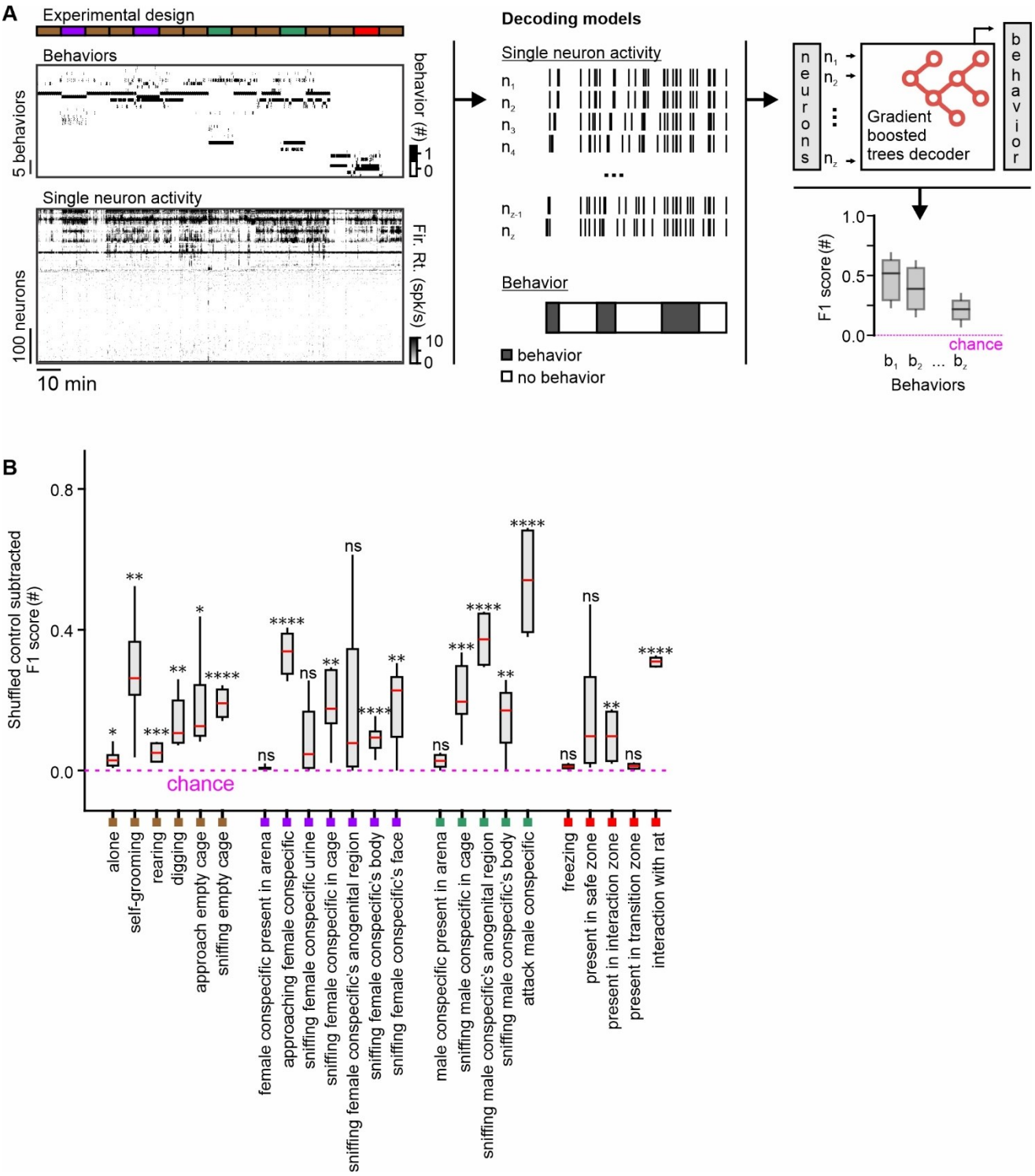
A
Experimental design
Behaviors
5 behaviors
behavior (#)
1
0
Single neuron activity
100 neurons
Fir. Rt. (spk/s)
10
0
10 min
Decoding models
Single neuron activity
Behavior
behavior
no behavior
neurons
Gradient boosted trees decoder
behavior
F1 score (#)
1.0
0.5
0.0
chance
Behaviors
B
Shuffled control subtracted F1 score (#)
0.8
0.4
0.0
chance
alone
self-grooming
rearing
digging
approach empty cage
sniffing empty cage
female conspecific present in arena
approaching female conspecific
sniffing female conspecific urine
sniffing female conspecific in cage
sniffing female conspecific's anogenital region
sniffing female conspecific's body
sniffing female conspecific's face
male conspecific present in arena
sniffing male conspecific in cage
sniffing male conspecific's anogenital region
sniffing male conspecific's body
attack male conspecific
freezing
present in safe zone
present in interaction zone
present in transition zone
interaction with rat

830

**Fig. S10. Solitary, social and fear behavior actions can be decoded from hypothalamic single neuron activity using gradient boosted trees decoding models.** (**A**) Schematic of the analysis pipeline using gradient-boosted trees for binary decoding of behavior based on single unit activity. (**B**) Shuffled F1-score subtracted, k-fold cross-validated F1-score output of decoding behavior based on the gradient boosted trees decoders (box plots are made of points from the six recorded mice – each mouse contributing a single point unless a behavior was not expressed by an individual). In box-and-whisker plots, center lines indicate medians, box edges represent the interquartile range, and whiskers extend to the minimal and maximal values.

ns: statistically not significant, *$P < 0.05$, **$P < 0.01$, ***$P < 0.001$, ****$P < 0.0001$. In box-and-whisker plots, center lines indicate medians, box edges represent the interquartile range, and whiskers extend to the minimal and maximal values. See also Fig. S11. Figure relevant to Fig. 3 and 5.

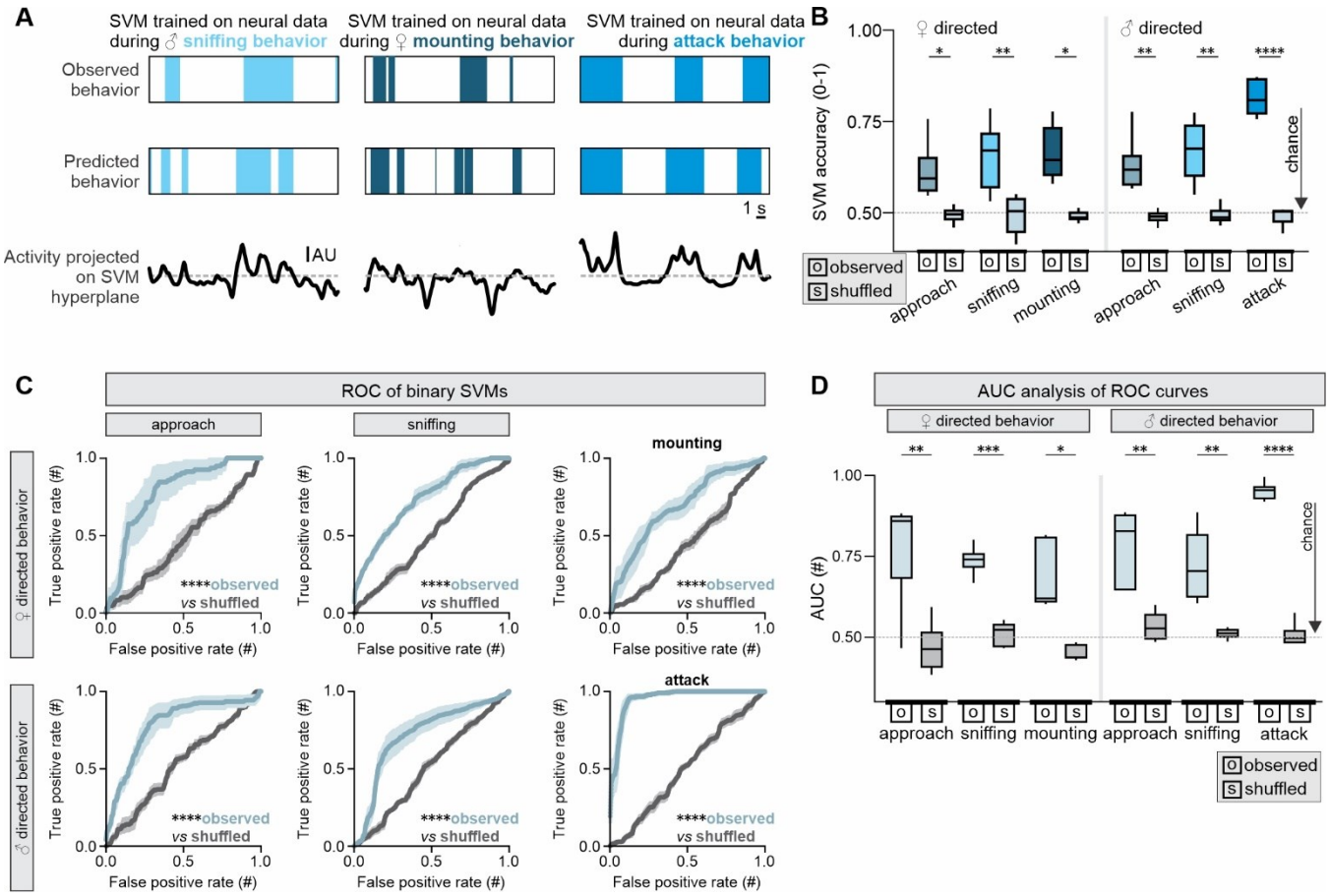


**Fig. S11. Intermale and male-female social behavior actions can be decoded with high accuracy by support vector machines decoding models.** (**A**) Example accuracy of three decoders on the test data of three social behaviors, and activity projected on the SVM hyperplane. (**B**) Decoder accuracy on behaviors of interest (n = 6 mice). (**C**) ROC curves on the observed and shuffled data (n = 6 mice). (**D**) Quantification of the area under the curve of the ROC curves shown in panel (**C**).

**P* < 0.05, ***P* < 0.01, ****P* < 0.001, *****P* < 0.0001. Statistical comparisons of the data shown in panel (D) were performed against each group's shuffled control using paired two-tailed *t*-test. In box-and-whisker plots, center lines indicate medians, box edges represent the interquartile range, and whiskers extend to the minimal and maximal values. See also Fig. S10. Figure relevant to Fig. 3 and 5.

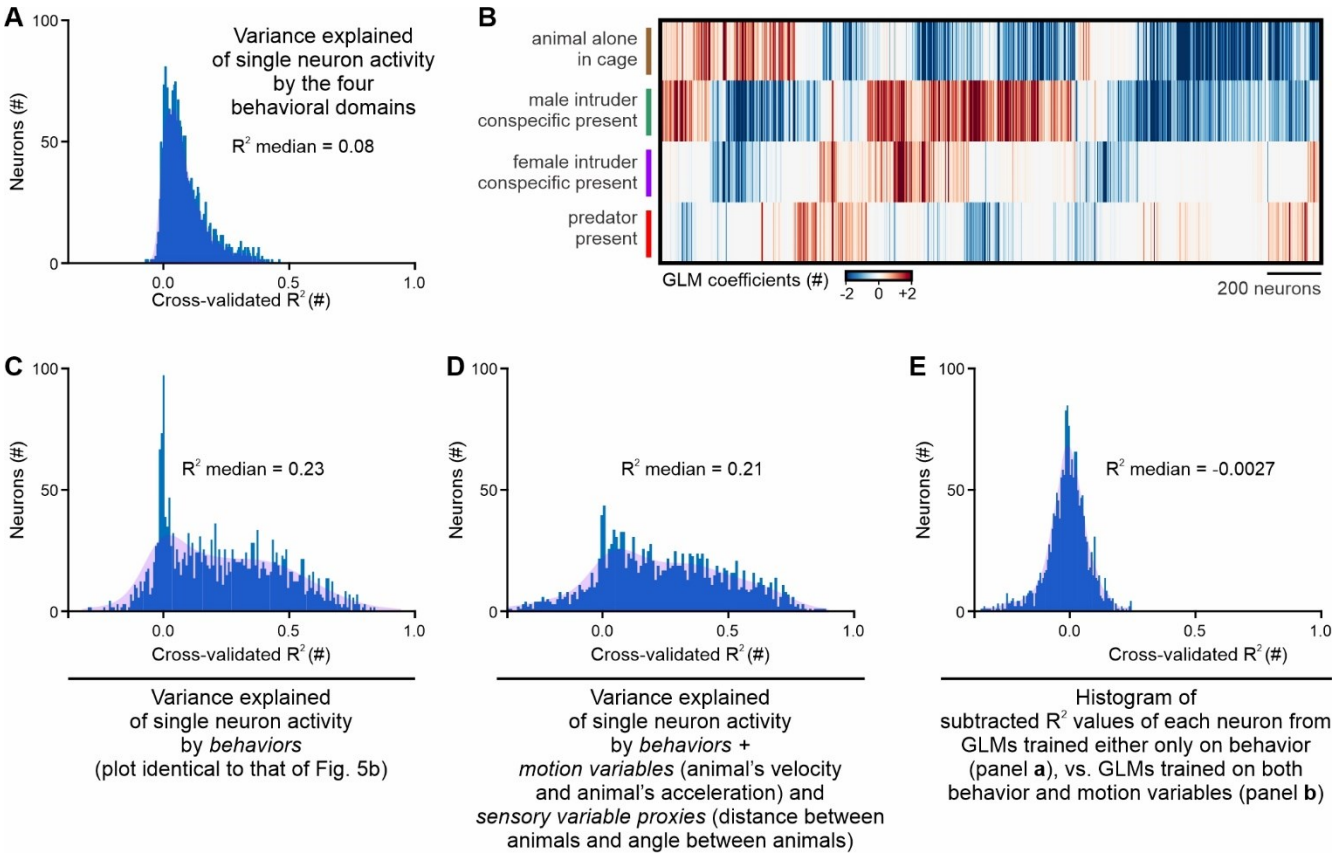


**Fig. S12. Single neuron activity variance explained by behavioral domains, motion variables, and sensory proxy signals.** (**A**) Variance explained (cross-validated, shuffled data $R^2$ subtracted, $R^2$) of single-neuron activity (n=6 mice, 2347 neurons) based on the four behavioral domains of interest, solitary, male intruder in arena, female intruder in arena, and predator in arena. Output of Poisson-GLM. (**B**) Behavioral domain coefficients on single neurons recorded across all mice (n=6 mice). (**C**) Variance explained (cross-validated, shuffled data $R^2$ subtracted, $R^2$) of single-neuron activity (n=6 mice, 2347 neurons) based on forty-two annotated behaviors. (**D**) Variance explained (cross-validated, shuffled data $R^2$ subtracted, $R^2$) of single-neuron activity (n=6 mice, 2347 neurons) based on forty-two instinctual behaviors and four motion variables, i.e., animal's velocity, animal's acceleration, distance and angle between animals. (**E**) Difference in the variance explained by behavior vs. behavior + motion variables. Histogram generated by subtraction of each neuron's $R^2$ generated via GLMs trained and tested only using annotated behaviors as predictor variables, against the neuron's $R^2$ generated via GLMs trained

865 and tested using annotated behaviors and motion variables as predictors. The peak around $R^2$=0, is
866 suggestive that motion variables explain little if any of the variance of hypothalamic single neuron activity.
867 Figure relevant to Fig. 5.

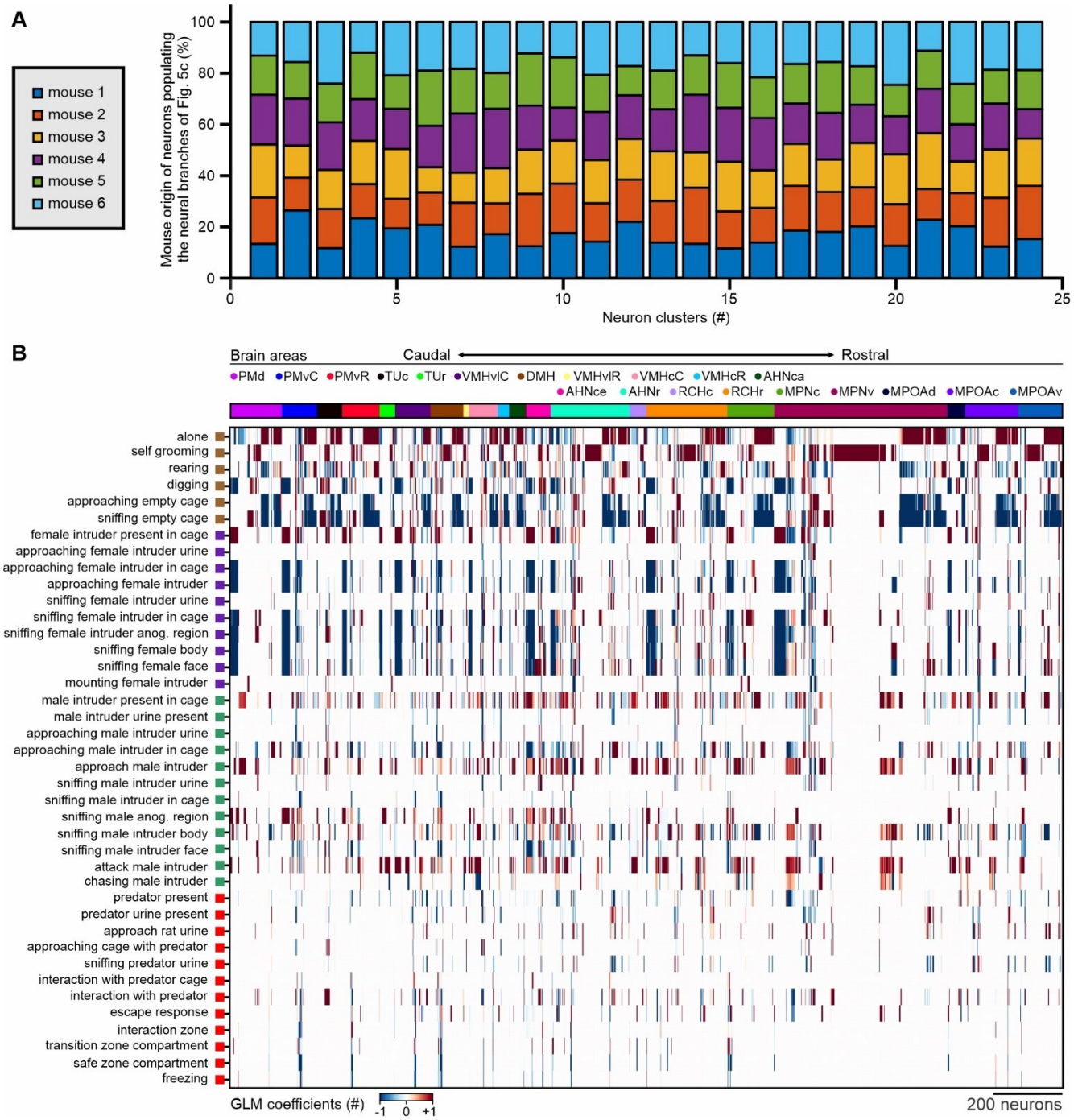


**Fig. S13. Contibution of neurons per mouse to the composition of clusters shown in Fig. 5C, and sorting of neurons based on their anatomical coordinates across the rostro-caudal hypothalamic axis (also related to Fig. 5C).** (**A**) Neuron contribution from each of the recorded mice to the neural branches presented in Fig. 5C. (**B**) Sorting neurons based on their spatial coordinates (as compared to the agglomerative linkage clustering-based sorting using behavior coefficients shown in Fig. 5C).

# Materials And Methods

880 **Experimental animals**

881 All experiments involving the use of living animals or their tissues adhered strictly to the guidelines set
882 by the National Institutes of Health (NIH). They were conducted under the approval of both the
883 Institutional Animal Care and Use Committee and the Institutional Biosafety Committee at the California
884 Institute of Technology (Caltech). Swiss Webster (CFW) mice (Crl: CFW [SW]), C56BL/6NCrl mice, and
885 Long-Evans (Crl:LE) rats were purchased from Charles River US. In all behavioral and resident-intruder
886 assays, wild-type mice from the C56BL/6NCrl strain were used (sourced from Charles River
887 Laboratories). Experimental animals were provided with additional enrichment and running wheels in
888 their cages, were maintained in good health, and were monitored by the local veterinarian. Housing
889 conditions for the mice were carefully monitored. Ventilated micro-isolator cages were maintained in an
890 environment with stable temperature (23$^{o}$C) and humidity (55-60%). A reverse light-dark cycle of 12 hours
891 each was used, and animals were provided unlimited access to food and water. The cages were cleaned
892 and changed once a week on a specific day and no experiments were conducted within two days of a
893 cage change.

894

895 **Selection of animals for experiments**

896 *In vivo* electrophysiology data were collected from six Swiss-Webster mice (out of 11 implanted animals
897 generated in a single cohort) and are reported here. Mice were selected for combined electrophysiology
898 and behavior experiments based on the following criteria: (1) recovered within two days to pre-
899 implantation baseline behaviors. (2) expressed the majority of instinctual behaviors on the experimental
900 days; and (3) identified single neurons did not show drift across experimental sessions.

901

902 **Surgical methods**

903 All surgical and behavioral procedures adhered to the standards set by the National Institutes of Health
904 and received approval from the Institutional Animal Care and Use Committee at Caltech. Male Swiss

905 Webster mice, aged between 3-4 months, were used for neural recordings during behavior. Male mice
906 were used to avoid potential confounding effects of the estrous cycle in female mice.
907 Prior to surgery, mice were provided with medicated food cups (MediGel CPF, Clear H20 74-05-5022),
908 containing carprofen, for two days. Throughout the surgical procedure, mice were kept anesthetized with
909 isoflurane. The initial steps included removing the skin and clearing any underlying connective tissue.
910 The tissue surrounding the skull edges was securely adhered with Vetbond (Santa Cruz Biotechnology,
911 cat. no. sc-361931), and the skull surface was prepared by being scraped, dried, and textured.
912 A custom boomerang-shaped titanium head bar was affixed to the occipital bone of the skull, and a hole
913 for the ground screw was carefully drilled, placing the screw above the right prefrontal cortex. Optibond
914 Solo Plus (Kerr, cat No. 31514) was applied to the skull and cured under UV light. Charisma (Net32, cat.
915 No. 66000085) was employed to establish a base for the implant and to reinforce the area around the
916 ground screw.
917 With the help of a dental drill, eight 100 μm holes were made above the somatosensory cortex. These
918 holes were designed to accommodate the eight shanks of the silicon probe, aimed at penetrating the
919 deep brain. The entire silicon probe assembly, including the probe and headstage, was placed in the
920 stereotax. Post-application of DiD' (ThermoFisher Scientific, cat. no. D7757) on the posterior to the
921 electrode surface of each shank, the probe was gently lowered into the brain at a speed of 6 μm/sec
922 resulting to an insertion time of fifteen minutes. Higher insertion speeds negatively impacted post-surgery
923 recovery and neuron yield per mouse.
924 The precise coordinates for probe insertion and the angle of attack were adapted for each mouse
925 accommodating idiosyncratic differences in cortical vasculature identified post-drilling, and enabling the
926 recording of the same deep brain structures. The ground wire was soldered to the ground screw and
927 Metabond cement was used to secure the probe and headstage to the skull. The entire assembly was
928 wrapped in Kapton Tape (ULINE S-7595), followed by a recovery period typically extending to two weeks.
929 Post-surgery, mice were individually housed, and additional enrichment elements were provided. Daily
930 monitoring was performed to evaluate locomotion and the expression of behaviors (self-grooming, rearing

931 and digging). Between the second and third weeks, mice were acclimatized in test arenas to examine
932 their natural movement and the manifestation of thigmotaxis in the open field test, among other behaviors.
933
934 **Behavioral tests**
935 All behavioral tests were performed during the dark phase and under dim red light between 2 h after the
936 initiation of the dark phase and three hours before the initiation of the light phase. Mice were acclimated
937 to the testing behavior room for a minimum of one hour before testing with *ad libitum* access to food and
938 water. Videos were recorded using the GS3-U3-51S5C-C 2/3" FLIR Grasshopper®3 USB 3.0 Color
939 Camera, at thirty frames per second. Video acquisition was triggered through a TTL signal provided to
940 the *trigger*-in GPIO port of the camera, by the neural data acquisition software Allego – NeuroNexus'
941 proprietary software for data acquisition. Timestamps for frames were collected and recorded as an
942 auxiliary signal through the software Allego and NeuroNexus' data acquisition box (SmartBox Pro).
943
944 **Resident–intruder (RI) test**
945 The resident's cage was not cleaned for a minimum of 2 days before the behavioral test. A single male
946 or female intruder was introduced per testing session. A ten-minute habituation period was allowed and
947 recorded, and was followed by the introduction of a freely moving intruder for ten minutes or an intruder
948 within a perforated cage. Video and neural data acquisition continued for ten minutes following the
949 removal of the intruder. Intruders were of the C57BL/6N background, and were either intact males, or
950 intact females in the estrus phase of the estrous cycle (stage of cycle was defined by inspection of vaginal
951 smears, and the cycle of individual female intruders was followed for three consecutive days prior to the
952 day of the experiment). Behaviors during the RI test were video recorded using a top view camera, and
953 were manually annotated using BENTO (*70*) (https://github.com/neuroethology/bentoMAT).
954
955
956

957 **Predatory fear (PF) behavioral assay**

958 A custom four-chamber arena was used to present a caged-predator. All but the front sides of the cage
959 of the predator were opaque white colored, with the exception of the front side that was clear and the
960 wall was perforated evenly with square holes five square millimetres in size placed fifteen millimetres
961 apart (center to center). This design aims to allow diffusion of pheromonal cues that may affect the
962 behavior of pray animals. Other than the chamber containing the predator, the arena includes three other
963 chambers: i) the interaction zone chamber that allows the mouse to sniff the predator and interact with
964 the cage before, during and after the presence of the rat in the arena. ii) The transition zone chamber
965 that allows the mouse to move between the proximal and furthest away chambers from the rat, and iii)
966 the safe zone chamber, that places a large distance between the mouse and the predator. The validation
967 parameters of this custom experimental design are presented in extended data figure four.

968

969 **Behavior annotations and quantification of behavior**

970 Behavior videos were manually annotated using BENTO (*70*) (freely available software package:
971 https://github.com/neuroethology/bentoMAT). A total of forty-three behaviors during the resident intruder
972 and predatory fear assays were annotated. The behavioral videos were loaded into MATLAB and a
973 trained individual blind to the experimental design annotated the videos frame-by-frame for all behavior
974 actions. Behavior annotations were then further edited by an expert (author: S.S.) who was not blind to
975 the experiment conditions. Imaging frames were spatially downsampled by a factor of two, a modification
976 that we recognize to not influence identification of the behaviors of interest and that facilitates smoother
977 processing of the videos by BENTO (*70*) in MATLAB. Behavior features including velocity, acceleration,
978 distance and angle between animals were calculate using DeepLabCut (*38*), and custom MATLAB
979 routines.

980

981 ***In vivo* electrophysiology**

982 *In vivo* electrophysiology recordings were performed in freely moving mice, using chronic silicon probe
983 implants. All extracellular recordings were conducted across the rostro-caudal hypothalamic axis of the
984 left hemisphere. Recordings were performed using a 256-channel custom-built for this specific project
985 silicon probe, the A8x32-Poly2-7.5mm-25s-325-177 NeuroNexus probe, now commercially available.
986 This specific probe includes eight shanks evenly spaced by 325 μm, and each shank at its lower end
987 contains two columns of electrodes, each electrode with 25 μm distance from the next. The recording
988 area of each electrode was designed to 25 $\mu m^2$. The length of each shank was 7.5 mm to enable the
989 probe to reach the model ventral nuclei of the deep brain in the hypothalamus.
990 Electrophysiology data was collected with Allego (proprietary software of NeuroNexus, recently updated
991 to Radiens [https://www.neuronexus.com/products/software/radiens/]), at 20 kHz sampling frequency.
992 Kilosort 2.5 was used for spike sorting (*30*), and we refined its output with manual curation of the results
993 through phy: https://github.com/kwikteam/phy. Neurons that exhibited drift or units that had multiunit
994 activity were excluded. To assess the neural recordings and perform basic related analysis prior to
995 exploring the data relevant to behavior, we used MATLAB code that can be found here:
996 https://github.com/cortex-lab/spikes. The quality of recordings was assessed through quantification of the
997 event rate, i.e., the frequency of spikes that are higher than the background noise level. We considered
998 an 'event' to be any occurrence that matches in time (less than 1 millisecond) and space (50 millimetres
999 in radius) and that has a strength that is at least six times greater than the median absolute deviation
1000 (MAD) (*71*). Secondly, for unit quality assessment we computed and plotted the signal-to-noise ratio
1001 (SNR) for each event. Event detection (spikes), spike amplitudes, and firing rates were further inspected
1002 with custom MATLAB routines (https://github.com/jenniferColonell/Neuropixels_evaluation_tools).
1003

1004 **Whole-brain Imaging and Anatomical Registration of Probe Electrodes**

1005 Brains that had been cleared were imaged using the LaVision BioTec UltraMicroscope II in dibenzylether
1006 at two different wavelengths: 488 nm (which creates green autofluorescence) and 632 nm (which allows
1007 for the visualization of electrode tracks through the DiD dye, a fixable, lipophilic far-red dye that remains

1008 stable even in dehydrated conditions). The imaging was done using an Olympus MVPLAPO 2X/0.5
1009 objective, a 5 μm step size, approximately 5 μm pixel size (at 0.8X magnification), and a single light sheet
1010 focus. The imaging only included the hemisphere of the brain where the electrode tracks were located,
1011 and it was carried out in a sagittal orientation.
1012 Images obtained from the green and far-red channels were subsequently downsampled to a 25 μm
1013 resolution by means of averaging. The green channel was then matched to the Allen Brain Atlas CCFv3
1014 autofluorescence atlas with a 25 μm resolution using a two-step process: an initial affine transformation
1015 followed by a non-linear transformation carried out in Elastix. Previous studies have demonstrated that
1016 this method has an average registration error of about 4 voxels (or 100 μm). The same transformation
1017 process was also applied to the red channel.
1018 Electrode tracks were traced in the registered space using a custom R code that is based on AllenCCF
1019 (https://github.com/cortex-lab/allenCCF). This was done after electrophysiological recordings were made
1020 following the placement of a chronic implant that targeted the full anterior-posterior length of the
1021 hypothalamus.
1022 For the final analysis, brain regions were organized into twenty distinct groups based on the Allen Brain
1023 Atlas hierarchy. The specific location of each unit was determined based on where that unit produced the
1024 highest amplitude on the electrode. The location along each electrode was transformed into the Allen
1025 Brain Atlas space according to the orientation and position of the traced electrode track for each
1026 recording. The final part of allocating each electrode to a hypothalamic region was performed manually,
1027 to further improve the output of the earlier-mentioned process. For each mouse, a unique spatial map of
1028 electrodes/hypothalamic brain areas was defined and was later used to assign individual extracellular
1029 units to specific anatomical regions.
1030

1031 ***k*-means clustering**

1032 The variance explained by a clustering solution in the context of the *k*-means algorithm reflects the
1033 proportion of the total variance in the dataset that is "captured" by the centroids of the clusters. In other

words, it indicates how well the centroids represent the data. For computing the variance explained is we used the sum of squared distances between data points and their assigned cluster centroids. The more the variance explained, the closer the data points are to their respective centroids, and hence the better the clustering solution. Specifically, we calculated within-cluster sum of squares (WCSS). After performing *k*-means clustering we obtained the cell indices, which provide the cluster assignments for each data point, and the centroids for the clusters. The sum of squared distances of each point to its cluster centroid gives us the WCSS. We then iterated over all data point. For each point, we calculated the squared Euclidean distance between the point and its assigned centroid and summed these squared distances. We then computed the total sum of squares (TSS). i.e., the sum of squared distances of each point from the overall mean of the data. The variance explained by the clustering solution can be found by subtracting the WCSS from the TSS and then dividing by the TSS. Note that as the number of clusters *k* increases, the WCSS tends to decrease (each point can be closer to its centroid), but there's usually a diminishing return. This is often visualized with an "elbow plot," where the rate of decrease in WCSS slows down after a certain number of clusters, indicating a potential good choice for k.

**GLM output – functional vs. spatial distribution of clusters**

Neuronal cluster data was analyzed to determine its relationship with four predefined behavioral categories. For each cluster, its activity was averaged across specific row ranges corresponding to each category. Negative activity was disregarded, and data was normalized using the z-score to mitigate outlier effects. The entropy was computed for each cluster based on its normalized activity distribution across behavioral categories. Entropy was utilized to quantify the distribution of each neuronal cluster's activity across the four behavioral categories. After averaging the activity for each category and normalizing these averages to form a probability distribution, the entropy was computed using the formula for a discrete probability distribution. This measure provided insights into whether a cluster's activity predominantly aligned with specific behavioral categories (low entropy) or was distributed across multiple categories (high entropy). For spatial analysis, a 'center of mass' approach was employed to gauge the

1060 distribution of each cluster's activity across 20 assumed brain regions. Both the functional (behavioral
1061 category-based) and spatial distributed-ness of each cluster were then visualized using a scatter plot.
1062

1063 **Decoding Analysis**

1064 Gradient boosted trees: neuronal data (spike rates, binned at 100 ms) was smoothened through
1065 convolution with a Gaussian kernel of 10 timesteps (1 second). The data to the decoder was then made
1066 recurrent by creating a temporal window of size ten at each given timestamp. The data was then flattened
1067 before decoding. The data was analyzed using five-fold cross-validation. Each behavior was decoded
1068 individually based on the activity of all neurons. Folds were created by determining the onsets of the
1069 behavior and then creating a temporal window of the length of the behavior before its onset. All events
1070 were concatenated, and cross-validation was performed on the resulting data. The decoding was
1071 performed using gradient-boosted trees (*72, 73*) (depth of 3, 50 estimators, lr = 0.01). Performance was
1072 evaluated by calculating the cross validate, shuffled data subtracted F1-score per behavior. For each
1073 behavior, we calculated the maximum performance within a specific temporal jitter (10 timesteps). We
1074 then averaged performances across animals.

1075 Support Vector Machines: To assess if single neuron activity holds information about specific social
1076 actions, we trained a unique binary linear decoder for each behavior action, to predict whether or not the
1077 behavior was taking place. To ensure the behavior's representations weren't mixed with the
1078 representations of the intruder's gender, we created separate decoders for behaviors directed towards
1079 males and females. During times when the behavior of interest was not being exhibited, we under-
1080 sampled the negative training data to balance the number of positive and negative training examples.
1081 We then used these binary labels alongside their matching activity vectors to train a linear SVM decoder.
1082

1083 **Code Availability**

1084 The code used for analysis in this study is available upon request from the first author
1085 (stefanos.stagkourakis@gmail.com).